fibrous tissue, with the exception of the ulcerous cavities and calcifications. However, the original thickness of the fibrous cap of ruptured plaques was unknown. Therefore, in this study, fibrous caps with various thicknesses were considered for the same plaque. Previous in vitro study (19) of human atherosclerotic materials has shown that fibrous caps usually fracture when the static stress exceeds 300 kPa. Therefore, the critical value for fibrous cap thickness, under which the stress on the fibrous cap would exceed 300 kPa, was also calculated for each plaque. This critical thickness was obtained with the abovementioned computer simulation of finite element models. When the critical fibrous cap is thin, it means that the plaque therefore seemed to be less vulnerable. The data were then used to conduct a computational stress analysis using the finite element model for the purpose of color mapping the longitudinal stress distribution, which was superimposed onto the original IVUS images.

This study was approved by the Institutional Review Board of the Hospital of Yamaguchi University School of Medicine. All patients provided signed informed consent to participate in the study before IVUS was performed.

RESULTS

Study of vessel models. This study showed the longitudinal stress distribution within plaques using a color-coded representation. Figure 2A illustrates the longitudinal distribution of equivalent stress within a hill-like homogeneous plaque model by use of relative color mapping. The concentration of equivalent stress could be observed at the top of the plaque hills, as well as at its shoulders. When there was a distortion of plaque shape, the stress was concentrated not only at the summits and shoulders, but also at dips in the irregular surfaces of plaque hills. There was a negative relationship between equivalent stress and luminal stenosis (Fig. 2B). When there was a remodeling of the vascular diameter at a constant maximum plaque thickness, the equivalent stress at the plaque surface of arteries with expansive remodeling was greater than that of arteries with constrictive remodeling (Fig. 2C).

When there was a lipid core, the stress was particularly concentrated at a localized surface area just above the lipid core (Fig. 3). The size of the lipid core had no influence on the surface stress value, given that the thickness of the fibrous cap

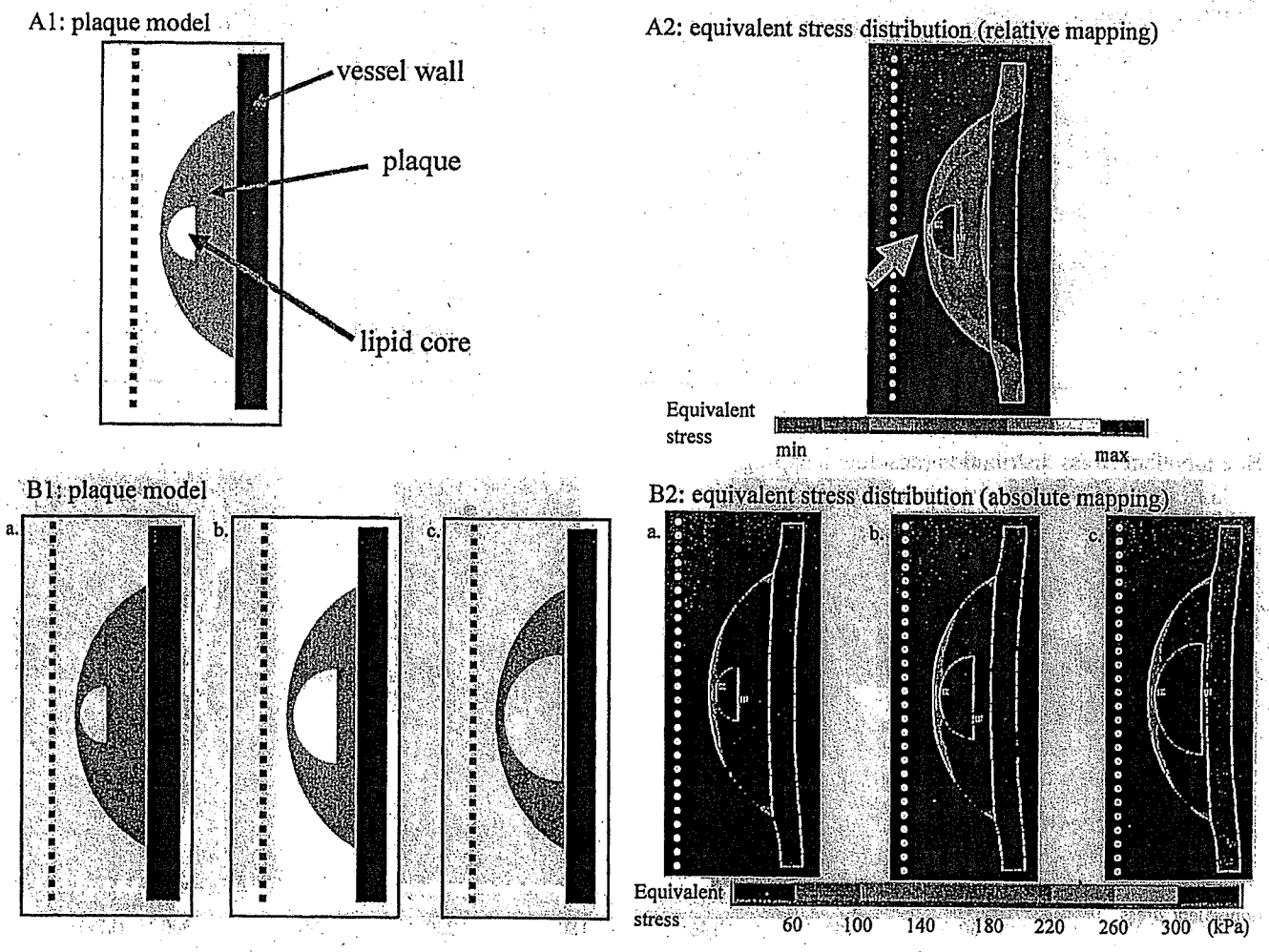

Figure 3. Effect of lipid core on stress distribution. The arrow indicates the point of stress concentration at a localized surface area just above the lipid core (**A2**). The size of the lipid core did not influence the value of the surface stress (**B2**), provided the fibrous cap thickness remained constant. (**A1, B1**) Plaque models used. (**A2, B2**) Mapping of stress distribution of the corresponded model.

remained constant. However, the thickness of the fibrous cap exerted a great impact on the surface equivalent stress of the plaque, namely, the thinner the fibrous cap, the greater the surface equivalent stress, given that the size of the lipid core remained constant (Fig. 4). In this idealized model, the peak equivalent stress reached beyond the empirical critical level leading to plaque rupture, when the fibrous cap was thinner than 80 μm. Superficial calcifications led to a decrease in surface stress, whereas calcification at the bottom of the plaque exerted no influence on the surface equivalent stress value. As in Figure 5, a superficial calcification adjacent to the lipid core attenuated the peak stress value at the plaque surface just above the lipid core. There was an inverse relationship between the surface equivalent stress and the thickness of the fibrous cap. The stress value increased dramatically when the fibrous cap was thinner than 80 μm. However, when there was a surface calcification near the lipid core, the surface equivalent stress was smaller with the same fibrous cap thickness, such that the inverse relationship shifted leftward and downward (Fig. 6).

IVUS study. Figure 7 shows representative examples of the color mapping of longitudinal stress distribution using longitudinal IVUS images. In case 1, the critical thickness of the fibrous cap leading to rupture was 50 μm, whereas this value was 10 μm in case 2. In case 2, there was a superficial calcification close to the rupture point. Table 2 shows the profile of the 15 ruptured plaques analyzed. The IVUS study showed that the critical thickness of fibrous caps leading to rupture varied between <10 μm and 200 μm.

DISCUSSION

This study was the first showing the longitudinal structural determinants of plaque vulnerability by use of a simplified computational analysis of stress distribution within atherosclerotic plaques using vessel models and three-dimensional intravascular ultrasound imaging. Furthermore, this study also showed that the critical thickness of fibrous caps leading to rupture varied substantially with differences in plaque structure, especially with differences in the degree of calcification.

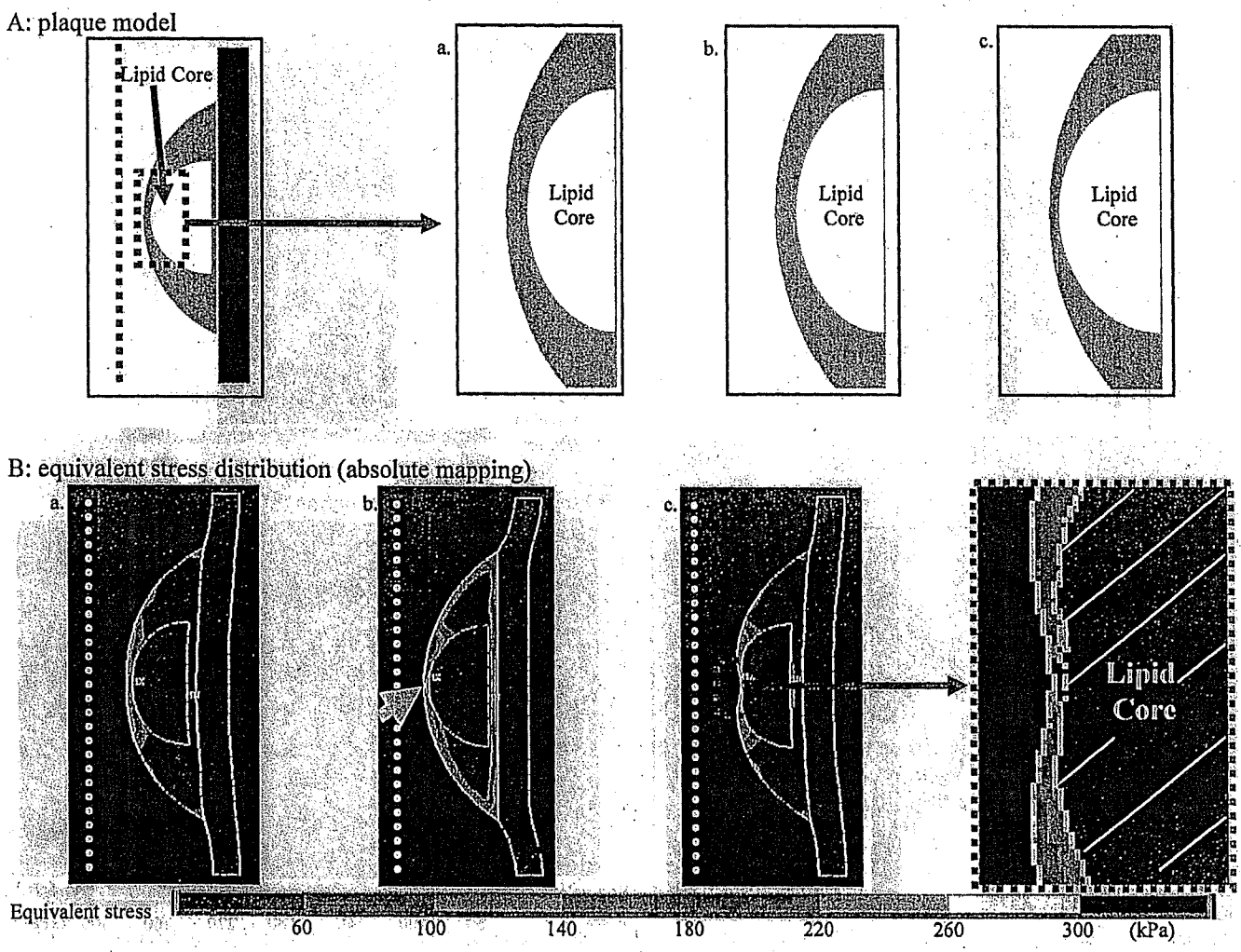

Figure 4. Effect of fibrous cap thickness (a, 90 μm; b, 80 μm; c, 40 μm) on stress distribution. When the fibrous cap was thinner than 80 μm, the stress was markedly elevated (arrow). (Aa, Ab, Ac) Plaque models used. (Ba, Bb, Bc) Mapping of stress distribution of the corresponded model.

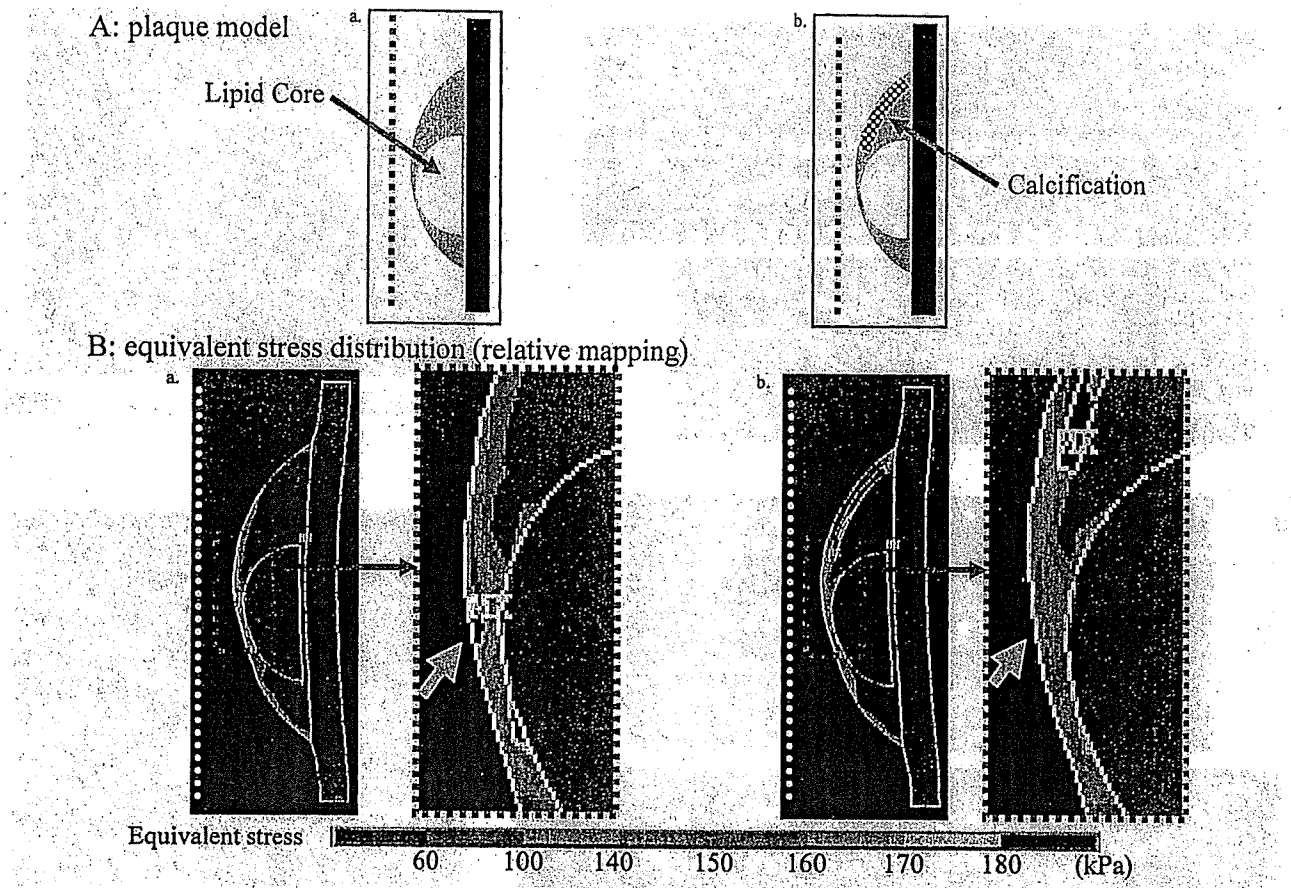

Figure 5. The effect of surface calcifications on the distribution of stress in the surrounding tissue. The size and the place of the lipid core remained constant. A superficial calcification adjacent to the lipid core attenuated the peak stress value at the plaque surface just above the lipid core (arrow). **(Aa, Ab)** Plaque models used. **(Ba, Bb)** Mapping of stress distribution of the corresponded model.

Plaque size, shape, vessel remodeling, and plaque stress. Previous cross-sectional structural analyses of plaque stress distribution have shown that the shoulder regions of eccentric plaques are likely to exhibit stress concentration, leading to a susceptibility to rupture (13). However, the results of this study indicated that longitudinal plaque shape is also important for predicting the location of stress concentration within plaques.

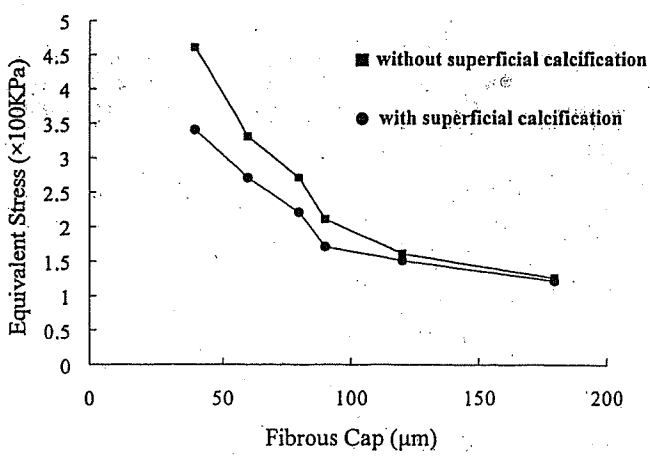

Figure 6. Effect of superficial calcifications on the relationship between the fibrous cap thickness and the peak equivalent stress at the plaque surface. The equivalent stress increased dramatically when the fibrous cap thickness became <80 μm. This increase shifted leftward and downward when there was a superficial calcification close to the area of interest.

Our study showed that increasing either plaque volume or the severity of stenosis decreased the degree of stress concentration. These findings were compatible with those of a previous cross-sectional structural analysis of plaques (13). According to the LaPlace law, the tensile stress on the wall of a luminal structure is correlated with luminal pressure and diameter, and is inversely related to the thickness of the wall. Increasing plaque volume thus increases the thickness of a wall and decreases the luminal diameter (unless there is vessel remodeling), thereby leading to a decrease in the surface stress of the plaque. The present results may therefore account for previous serial angiographic analyses showing that the culprit lesion before the acute event frequently had <50% diameter stenosis (3–8). Based on recent IVUS studies, it is likely that plaque regression or less progression that may not lead to stress attenuation is associated with a decrease in the risk of future cardiac events (9–11). Therefore, this paradoxical consequence could be attributed to simultaneous changes in plaque composition and fibrous cap thickness.

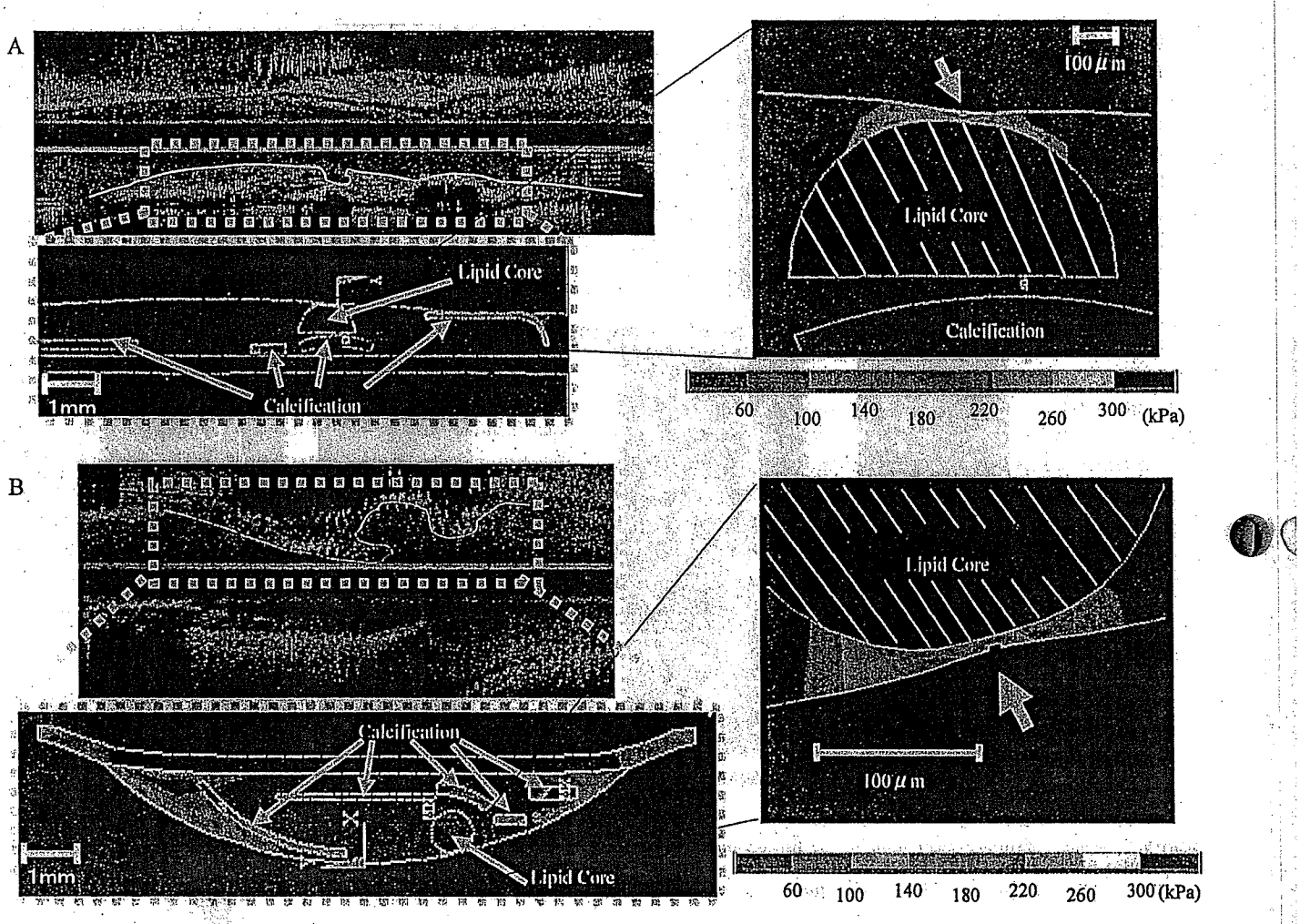

Figure 7. Representative examples of the three-dimensional IVUS images and the color mappings of longitudinal stress distribution. The arrows show rupture points. In case 1, the critical thickness of the fibrous cap in terms of rupture was 50 μm **(A)**. However, the thickness in case 2 had to be reduced to <10 μm to reach the critical point in terms of plaque rupture **(B)**. Thus, case 2 seemed to represent a less vulnerable plaque than case 1, although the fibrous cap thickness was the same. **(A)** Case 1; **(B)** case 2.

Table 2. Ruptured Plaque Characteristics Detected by IVUS and Its Simulated Critical Fibrous Cap Thickness

Case	Coronary Artery	Longitudinal Plaque Length	Plaque Thickness	Vessel Diameter	Ulcer Diameter	Superficial Ca	D (mm)	Deep Ca	Critical Fibrous Cap Thickness (μm)
1	LAD	14.6	2.6	5.2	3.1	+	0.8	+	<1
2	RCA	21.0	1.9	4.1	3.2	+	0	+	40
3	LAD	40.0	1.7	4.6	1.8	+	2.4	+	50
4	LAD	12.3	1.2	4.9	2.1	−	−	−	200
5	RCA	26.4	2.0	4.1	0.8	−	−	+	<10
6	LAD	13.2	2.1	5.1	1.7	+	0.7	+	20
7	LAD	5.9	1.2	4.0	0.9	+	2.0	+	15
8	LAD	5.3	1.4	3.6	0.7	−	−	+	60
9	LAD	5.1	1.3	3.3	0.8	−	−	+	60
10	LAD	15.5	2.6	4.0	1.5	−	−	+	<10
11	LAD	12.0	2.1	3.9	1.0	−	−	−	<10
12	LAD	8.2	2.1	3.5	1.8	−	−	+	<10
13	LAD	10.6	1.3	2.9	1.7	−	−	−	20
14	LAD	11.0	1.5	5.2	1.2	+	1.2	+	140
15	LAD	11.3	1.7	3.3	0.6	−	−	+	<10

Ca = calcification; D = distance between edge of superficial calcification and orifice of ulceration; IVUS = intravascular ultrasound; LAD = left anterior descending artery; RCA = right coronary artery.

In this study, when the plaque thickness remained constant, expansive remodeling led to a greater concentration of stress than did constrictive remodeling. Expansive remodeling is frequently observed as a compensatory process for an increase in plaque thickness. In such a case, stress attenuation by the increase in plaque thickness is canceled by expansion in vessel diameter, which consequently maintains or enhances stress value on the plaque surface. Therefore, the present results may be consistent with the findings of previous reports (9–12) showing that unstable plaques are usually associated with expansive remodeling.

Subintimal plaque structure and stress. The significant impact of decreases in fibrous cap thickness on stress concentration within plaques has been widely shown in various studies using postmortem pathological analyses and intravascular imaging modalities (4,13–17). Our findings showed that the stress on a fibrous cap was dramatically increased when its thickness was <80 μm. This value of 80 μm actually depends on the vessel diameter. The range of cap thickness of 60 to 100 μm corresponds to vessel diameters of 2.5 to 4mm. Previous empirical cross-sectional studies have shown that a fibrous cap thickness of less than 65 to 150 μm is critical in terms of the risk of plaque rupture (15,16,25–27). Therefore, the critical thickness of fibrous caps in terms of plaque rupture might be similar in both the cross-sectional and the longitudinal direction. However, the present study using longitudinal IVUS showed that the critical thickness of a fibrous cap leading to rupture varies greatly because of differences in the distribution of surrounding calcifications, even with the same vessel diameter. The involvement of calcification, and variabilities in plaque thickness and shape, may account for inconsistencies regarding the critical thickness reported in several previous studies, which has been shown to vary between 65 and 150 μm (15,16,25–27). The effect of vessel size would also account for a range of the critical thickness varying from 60 to 100 μm as noted above. Furthermore, our results suggest that the measurement of fibrous cap thickness alone is inadequate for identifying plaques vulnerable to rupture.

The presence of a lipid core was also an important factor in stress concentration, according to our study of the longitudinal vessel axis. However, increasing the size of a lipid core did not affect the surface stress of plaques, provided the thickness of the fibrous cap remained constant. These studies, as well as our own, may support the findings of previous reports showing that plaque rupture can be observed in the region of a fibrous cap, even in the presence of a very small lipid core (18,25,28).

Calcification is commonly found in atherosclerosis, but the role of calcification in plaque rupture is still unknown. Some studies indicate beneficial effects in stabilizing plaque (19,23,29), whereas some suggest its worsening effects to plaque vulnerability (30–34). In our study, calcification significantly affected the stress on fibrous caps that were either adjacent to or at a slight distance from calcifications. The exact mechanisms of the attenuation of stress by surface calcification are unclear.

Clinical implications. Although a variety of factors may participate in the process of plaque rupture, including hemodynamic shear stress (20), turbulent pressure fluctuations (35), transient compression (36), sudden increase in intraluminal pressure (37), rupture of the vaso vasorum (38), material fatigue (4,18,39), and cellular inflammatory reactions (3,4,22,40), this study suggests that assessment of stress concentration within a plaque along the longitudinal axis of a vessel is also important for identifying vulnerable plaques. Therefore, this approach may help identify vulnerable plaques or even help predict the point of future rupture.

Study limitations. To simplify the present finite element analysis, the materials were assumed to be isotropic, incompressible, and uniform solids. By assuming that plaques, lipids, calcium, and normal arterial walls could each be characterized by a single set of structural parameters, spatial and interspecimen variations within a particular component were not considered here. However, the assumptions used in this study have been widely accepted as allowable for the assessment of the biomechanical properties of atherosclerotic lesions (13,23). The model used in this study was a linear one, although almost all of the biomaterials have nonlinear properties. Actually, there are only limited data available with regard to the nonlinear biomechanical behavior of atherosclerotic lesions. Furthermore, in the present study, we examined factors affecting relative stress values and not exact absolute stress magnitudes.

In this study, we used an axisymmetric model, although clinical plaques are not always axisymmetric in geometry. The purpose of this study was limited to assess the longitudinal determinants of plaque vulnerability, but not cross-sectional determinants, which were already clarified in the numerous previous studies. Therefore, the axisymmetric model was used to exclude the cross-sectional determinants of stress distribution within plaques.

It was also assumed in this study that there were no shear stresses, torques, time-varying forces, or flow-related forces; only static blood pressure was considered to be acting on the lesion in the models. It has been documented that the effect of fluid shear stress is insignificant when compared with the effect of tensile wall stresses (19) as a direct component in plaque fracture dynamics. The estimation of stresses induced by static pressure load alone has already shown its usefulness in identifying stress concentration in human lesions (23), because the location of stress concentration does not significantly differ between the single static pressure model and the complex dynamic pressure model.

Reprint requests and correspondence: Dr. Takafumi Hiro, Department of Molecular Cardiovascular Biology, Yamaguchi University Graduate School of Medicine, 1-1-1 Minami Kogushi, Ube, Yamaguchi, 755-8505, Japan. E-mail: thiro@yamaguchi-u.ac.jp.

REFERENCES

1. Levin DC, Fallon JT. Significance of the angiographic morphology of localized coronary stenosis: histopathologic correlations. Circulation 1982;66:316–20.
2. Davies MJ, Thomas A. Thrombosis and acute coronary artery lesions in sudden cardiac ischemic death. N Engl J Med 1984;310:1137–40.
3. Shah PK. Mechanism of plaque vulnerability and rupture. J Am Coll Cardiol 2003;41 Suppl 1:15–22.
4. Falk E, Shah PK, Fuster V. Coronary plaque disruption. Circulation 1995;92:657–71.
5. Nobuyoshi M, Tanaka M, Nosaka H, et al. Progression of coronary atherosclerosis: is coronary spasm related to progression? J Am Coll Cardiol 1991;18:904–10.
6. Giroud D, Li JM, Urban P, Meier B, Rutishauer W. Relation of the site of acute myocardial infarction to the most severe coronary arterial stenosis at prior angiography. Am J Cardiol 1992;69:729–32.
7. Ambrose JA, Tannenbaum MA, Alexopoulos D, et al. Angiographic progression of coronary artery disease and the development of myocardial infarction. J Am Coll Cardiol 1988;12:56–62.
8. Little WC, Constantinescu M, Applegate RJ, et al. Can coronary angiography predict the site of a subsequent myocardial infarction in patients with mild-to-moderate coronary artery disease? Circulation 1988;78:1157–66.
9. Schoenhagen P, Ziada KM, Kapadia SR, Crowe TD, Nissen SE, Tuzcu EM. Extent and direction of arterial remodeling in stable versus unstable coronary syndromes: an intravascular ultrasound study. Circulation 2000;101:598–603.
10. Birgelen CV, Klinkhart W, Mintz GS, et al. Plaque distribution and vascular remodeling of ruptured and nonruptured coronary plaques in the same vessel: an intravascular ultrasound study in vivo. J Am Coll Cardiol 2001;37:1864–70.
11. Shoenhagen P, Ziada KM, Vince DG, Nissen SE, Tuzcu EM. Arterial remodeling and coronary artery disease: the concept of "dilated" versus "obstructive" coronary atherosclerosis. J Am Coll Cardiol 2001;38:297–306.
12. Smits PC, Pasterkamp KR, deJaegere PPT, Feyter PJ, Borst C. Angioscopic complex lesions are predominantly compensatory enlarged. Cardiovasc Res 1999;41:458–64.
13. Loree HM, Kamm RD, Stringfellow RG, Lee RT. Effects of fibrous cap thickness on peak circumferential stress in model atherosclerotic vessels. Circ Res 1992;71:850–8.
14. Nissen SE, Yock P. Intravascular ultrasound: novel pathophysiological insights and current clinical applications. Circulation 2001;103:604–16.
15. Maseri A, Fuster V. Is there a vulnerable plaque? Circulation 2003; 107:2068–71.
16. Virmani R, Kolodgie FD, Burke AP, Farb A, Schwartz SM. Lessons from sudden coronary death: a comprehensive morphological classification scheme for atherosclerotic lesions. Arterioscler Thromb Vasc Biol 2000;20:1262–75.
17. Davies MJ, Richardson PD, Woolf N, et al. Risk of thrombosis in human atherosclerotic plaques: role of extracellular lipid, macrophage, and smooth muscle cell content. Br Heart J 1993;69:377–81.
18. Richardson PD, Davies MJ, Born GV. Influence of plaque configuration and stress distribution on fissuring of coronary atherosclerotic plaques. Lancet 1989;2:941–4.
19. Huang H, Virmani R, Younis H, Burke AP, Kamm RD, Lee RT. The impact of calcification on the biomechanical stability of atherosclerotic plaques. Circulation 2001;103:1051–6.
20. Gertz SD, Roberts WC. Hemodynamic shear force in rupture of coronary arterial atherosclerotic plaques. Am J Cardiol 1990;66: 1368–72.
21. Hodgson JM, Reddy KG, Suneja R, Nair RN, Lesnefsky EJ, Sheehan HM. Intracoronary ultrasound imaging: correlation of plaque morphology with angiography, clinical syndrome and procedural results in patients undergoing coronary angiography. J Am Coll Cardiol 1993;21:35–44.
22. Lendon CL, Davies MJ, Born GV, Richardson PD. Atherosclerotic plaque caps are locally weakened when macrophage density is increased. Atherosclerosis 1991;87:87–90.
23. Cheng GC, Loree HM, Kamm RD, Fishibein MC, Lee RT. Distribution of circumferential stress in ruptured and stable atherosclerotic lesions: a structural analysis with histopathological correlation. Circulation 1993;87:1179–87.
24. Lee RT, Loree HM, Cheng GC, Lieberman EH, Jaramillo N, Schoen FJ. Computational structural analysis based on intravascular ultrasound imaging before in vitro angiography: prediction of plaque fracture locations. J Am Coll Cardiol 1993;21:777–82.
25. Ge J, Chirillo F, Schwedtmann J, et al. Screening of ruptured plaques in patients with coronary artery disease by intravascular ultrasound. Heart 1999;81:621–7.
26. Burke AP, Farb A, Malcom GT, Liang Y, Smialek J, Virmani R. Coronary risk factors and plaque morphology in men with coronary disease who died suddenly. N Engl J Med 1997;336:1276–82.
27. MacNeill BD, Lowe HC, Takano M, Fuster V, Jang IK. Intravascular modalities for detection of vulnerable plaque: current status. Arterioscler Thromb Vasc Biol 2003;23:1333–42.
28. Mann JM, Davies MJ. Vulnerable plaque: relation of characteristics to degree of stenosis in human coronary arteries. Circulation 1996;94: 928–31.
29. Alderman EL, Corley SD, Fisher LD, et al. Five-year angiographic follow-up of factors associated with progression of coronary artery disease in the Coronary Artery Surgery Study (CASS). J Am Coll Cardiol 1993;22:1141–54.
30. Raggi P, Callister TQ, Cooil B, et al. Identification of patients at increased risk of first unheralded acute myocardial infarction by electron-beam computed tomography. Circulation 2000;101:850–5.
31. Arad Y, Spadaro LA, Goodman K, Newstein D, Guerci AD. Prediction of coronary events with electron beam computed tomography. J Am Coll Cardiol 2000;36:1253–60.
32. Taylor AJ, Burke AP, O'Malley PG, et al. A comparison of the Framingham risk index, coronary artery calcification, and culprit morphology in sudden cardiac death. Circulation 2000;101:1243–8.
33. Schmermund A, Erbel R. Unstable coronary plaque and its relation to coronary calcium. Circulation 2001;104:1682–7.
34. Mintz GS, Pichard AD, Popma JJ, et al. Determinants and correlates of target lesion calcium in coronary artery disease: a clinical, angiographic and intravascular ultrasound study. J Am Coll Cardiol 1997; 29:268–74.
35. Loree HM, Kamm RD, Atkinson CM, Lee RT. Turbulent pressure fluctuations on surface of model vascular stenosis. Am J Physiol 1991;261:H644–50.
36. Binns RL, Ku DN. Effect of stenosis on wall motion: a possible mechanism of stroke and transient ischemic attack. Arteriosclerosis 1989;9:842–7.
37. Muller JE, Tofler GH, Stone PH. Circadian variation and triggers of onset of acute cardiovascular disease. Circulation 1989;79:733–43.
38. Barger AC, Beeuwkes R, Lainey LL, Silverman KJ. Hypothesis: vasa vasorum and neovascularization of human coronary arteries. A possible role in the pathophysiology of atherosclerosis. N Engl J Med 1984; 310:175–7.
39. MacIsaac AI, Thomas JD, Topol EJ. Toward the quiescent coronary plaque. J Am Coll Cardiol 1993;22:1228–41.
40. Davies MJ. Stability and instability: two faces of coronary atherosclerosis. Circulation 1996;94:2013–20.

Breast Disease: Clinical Application of US Elastography for Diagnosis[1]

Ako Itoh, MD
Ei Ueno, MD, PhD
Eriko Tohno, MD, PhD
Hiroshi Kamma, MD, PhD
Hideto Takahashi, PhD
Tsuyoshi Shiina, PhD
Makoto Yamakawa, PhD
Takeshi Matsumura, MS

Purpose: To evaluate the diagnostic performance of real-time free-hand elastography by using the extended combined auto-correlation method (CAM) to differentiate benign from malignant breast lesions, with pathologic diagnosis as the reference standard.

Materials and Methods: This study was approved by the University of Tsukuba Human Subjects Institutional Review Board; all patients gave informed consent. Conventional ultrasonography (US) and real-time US elastography with CAM were performed in 111 women (mean age, 49.4 years; age range, 27–91 years) who had breast lesions (59 benign, 52 malignant). Elasticity images were assigned an elasticity score according to the degree and distribution of strain induced by light compression. The area under the curve and cutoff point, both of which were obtained by using a receiver operating characteristic curve analysis, were used to assess diagnostic performance. Mean scores were examined by using a Student *t* test. Sensitivity, specificity, and accuracy were compared by using the standard proportion difference test or the Δ-equivalent test.

Results: For elasticity score, the mean ± standard deviation was 4.2 ± 0.9 for malignant lesions and 2.1 ± 1.0 for benign lesions ($P < .001$). When a cutoff point of between 3 and 4 was used, elastography had 86.5% sensitivity, 89.8% specificity, and 88.3% accuracy. When a best cutoff point of between 4 and 5 was used, conventional US had 71.2% sensitivity, 96.6% specificity, and 84.7% accuracy. Elastography had higher sensitivity than conventional US ($P < .05$). By using equivalence bands for noninferiority or equivalence, it was shown that the specificity of elastography was not inferior to that of conventional US and that the accuracy of elastography was equivalent to that of conventional US.

Conclusion: For assessing breast lesions, US elastography with the proposed imaging classification, which was simple compared with that of the Breast Imaging Recording and Data System classification, had almost the same diagnostic performance as conventional US.

[1] From the Department of Breast and Endocrine Surgery, Tsukuba University Hospital (A.I.), and Institutes of Clinical Medicine (E.U., E.T.), Basic Medical Sciences (H.K.), Community Medicine (H.T.), and Systems and Information Engineering (T.S., M.Y.), University of Tsukuba, Tsukuba, Japan; and Research and Development Center, Hitachi Medical Corporation, Kashiwa City, Japan (T.M.). Received September 30, 2004; revision requested December 3; revision received February 21, 2005; accepted March 15; final version accepted June 21. **Address correspondence to** A.I., Department of Surgery, Hitachi General Hospital, 2-1-1 Jonan-Cho, Hitachi City, Ibaraki-ken, 317-0077, Japan (e-mail: *ako.itou@ibabyo.hitachi.co.jp*).

Generally, breast cancer tissue is harder than the adjacent normal breast tissue. This property serves as the basis for some examinations, such as palpation, that are currently being used in the clinical assessment of breast abnormalities, as well as for elastography.

The principle of elastography is that tissue compression produces strain (displacement) within the tissue and that the strain is smaller in harder tissue than in softer tissue. Therefore, by measuring the tissue strain induced by compression, we can estimate tissue hardness, which may be useful in diagnosing breast cancer.

Elastography has been used clinically to examine a variety of breast lesions in patients, and it has been concluded that this modality may be useful for differentiating malignant from benign masses (1).

During elastography, it is assumed that the main displacement of tissue occurs in the longitudinal direction (ie, in the direction of the beam). This condition can be largely met by applying compression with a well-controlled stepping motor. With freehand compression, however, the influence of probe movement on the skin's surface in the lateral direction (so-called creep or slip) must be suppressed. A high-speed algorithm for estimating strain distribution is required for real-time measurement. In addition, an ideal elastography system will have a large dynamic range of strain for stable measurements that does not depend on the speed and extent of compression.

Three methods—that is, the spatial correlation method, the phase-shift tracking method, and the combined autocorrelation method (CAM)—have been introduced for measuring tissue strain at elastography. Although a head-to-head comparison of these methods is lacking, each method appears to have certain advantages and disadvantages (Table 1).

The spatial correlation method uses an ordinary two-dimensional pattern-matching algorithm to search for the position that maximizes the cross correlation between regions of interest (ROIs) that are selected from two images (one obtained before and the other obtained after deformation). This method can be used to demonstrate displacement in two dimensions (longitudinal and lateral), but the processing time is lengthy, which is a disadvantage for real-time assessment. The phase-shift tracking method is based on an autocorrelation method that is well known as a principle of color Doppler ultrasonography (US). As a result, this method can be used to rapidly and precisely determine longitudinal tissue motion because of phase-domain processing. Because of errors that are related to aliasing, the phase-shift tracking method fails when used to measure large displacements. In addition, this method poorly compensates for movement in the lateral direction, which is a disadvantage for freehand compression.

To overcome this problem, we developed a third method—the CAM (2–4). This method enables rapid and accurate detection of longitudinal displacement by using phase-domain processing without aliasing. Because lateral and elevational tissue movements are inevitable during palpation-like freehand manipulation of the probe, we modified the CAM to better demonstrate tissue displacement in these directions (5).

The dynamic range of strain that is estimated by using the extended CAM is 0.05%–5.00% (optimal dynamic range, 0.50%–2.00%); this method can compensate for up to about 4 mm of lateral slip (5). We have further developed this system for clinical breast examination.

Thus, the purpose of our study was to evaluate the diagnostic performance of real-time freehand elastography by using the extended CAM to differentiate benign from malignant breast lesions, with pathologic diagnosis as the reference standard.

Table 1

Comparison of Different Methods for Measuring Strain

Method	Processing Speed	Precision	Measureable Range of Strain	Sensitivity to Lateral Slip
Spatial correlation	Slow	Moderate	Large	Robust
Phase-shift tracking	Fast	High	Small	Weak
CAM	Fast	High	Large	Robust

Materials and Methods

Patients

This study was approved by the University of Tsukuba Human Subjects Institutional Review Board, and all patients provided informed consent. All data collection, analysis, and information submitted for publication were controlled by authors who were not employees of Hitachi Medical, which provided the equipment used for this study. We performed real-time freehand US elastography in 135 consecutive women who underwent evaluation for breast lesions (76 benign lesions and 59 malignant lesions) at Tsukuba University Hospital between March 22, 2002, and September 26, 2003; lesions were detected at conventional B-mode US and were classified as category 2–5 lesions according to the Breast Imaging Recording and

Published online before print
10.1148/radiol.2391041676

Radiology 2006; 239:341–350

Abbreviations:
ANDI = aberrations of normal development and involution
BI-RADS = Breast Imaging Recording and Data System
CAM = combined autocorrelation method
DCIS = ductal carcinoma in situ
ROI = region of interest

Author contributions:
Guarantors of integrity of entire study, E.U., E.T., T.S.; study concepts/study design or data acquisition or data analysis/interpretation, all authors; manuscript drafting or manuscript revision for important intellectual content, all authors; approval of final version of submitted manuscript, all authors; literature research, A.I., E.U., T.S.; clinical studies, A.I., E.U., E.T., H.K., T.S.; experimental studies, E.U., T.S., M.Y., T.M.; statistical analysis, E.U., H.T., T.S.; and manuscript editing, A.I., E.U., T.S.

See Materials and Methods for pertinent disclosures.

Data System (BI-RADS) criteria for US (6). Lesions were defined as areas in the breast tissue that were hypoechoic or isoechoic (compared with the subcutaneous fat) on B-mode images and included both mass-forming lesions and non–mass-forming lesions. At B-mode imaging, lesions that were clearly cystic or those that appeared as fat islands were not included.

Analyses were based on data from 111 patients in whom lesions measured no more than 30 mm in diameter and for whom cytologic or histologic diagnoses were obtained. Eight patients with lesions larger than 30 mm (one with a benign lesion and seven with malignant lesions) were excluded because these larger lesions could be diagnosed by using conventional diagnostic methods, such as cytology or biopsy. Furthermore, 16 patients (all with benign lesions) were excluded because no pathologic diagnosis was available. Overall, the remaining 111 patients had a mean age of 49.4 years (age range, 27–91 years). The 52 patients with breast cancer had a mean age of 52.9 years (age range, 29–91 years), and the 59 patients with benign lesions had a mean age of 47.4 years (age range, 27–73 years). This difference was not statistically significant according to the Welch test, which was used because pretest results (Bartlet test) did not show equal variance between groups. The diameter of malignant lesions (mean, 16.6 mm ± 6.1 [standard deviation]; range, 6–30 mm) was determined to be significantly greater than that of benign lesions (mean, 12.6 mm ± 6.2; range, 4–30 mm) by using the Student *t* test based on the pretest of variance equality (Bartlet test) ($P < .001$).

In all patients with benign or presumed benign lesions, we obtained follow-up data for a period of more than 1 year (ie, from the time of diagnosis to January 2005).

Pathologic Diagnoses

All diagnoses were made by a pathologist (H.K.) who had 20 years of experience in the pathologic analysis of breast cancer samples obtained with fine-needle aspiration cytology, needle biopsy, excisional biopsy, or radical surgery, all of which were performed according to the established criteria (7,8). Lesions were first classified as malignant or benign. The most prevalent malignant lesions were further divided into three subgroups according to the criteria of Japanese Breast Cancer Society (7). These subgroups included ductal carcinoma in situ (DCIS), invasive ductal carcinoma of nonscirrhous type, and invasive ductal carcinoma of scirrhous type. Similarly, the most prevalent benign lesions were divided into three subgroups on the basis of histologic features; these subgroups included intraductal papilloma, fibroadenoma, and aberrations of normal development and involution (ANDI) without fibroadenoma (eg, duct papillomatosis, sclerosing adenosis, and lobular hyperplasia) (7,8).

Equipment

Conventional US was performed by using a digital electronic scanner with a frequency range of 9–13 MHz (HDI 5000; Philips Medical Systems, Bothell, Wash) and an annular-array mechanical sector scanner with a frequency of 7.5 MHz (SSA-250A; Toshiba Medical Systems, Tochigi, Japan). Color Doppler US was performed in a subset of patients by using a digital electronic scanner with a speed range of 3.5 cm/sec (HDI 5000; Philips Medical Systems). Examinations were performed by a surgeon (E.U.) who had 26 years of experience in breast US or by a radiologist (E.T.) who had 20 years of experience in breast US. All elasticity images were obtained with a system that consisted of a digital US scanner (EUB-6500; Hitachi Medical, Tokyo, Japan) that was remodeled exclusively for this study and an external personal computer (Dell, Round Rock, Tex); images were collected by a surgeon (A.I.) who had 5 years of experience in breast US. The US probe was a 7.5-MHz liner electronic probe (EUP-L53; Hitachi Medical) equipped with a handmade stabilizer that could press evenly against a wide area, thereby minimizing the creep and rotation of the probe on the skin's surface. None of the patients in this study experienced adverse events from either conventional US or elastography.

Imaging Methods

Conventional US.—First, conventional US images of the breast were obtained. During our conventional examination, we obtained B-mode images first, and then color Doppler US was performed in patients with mass-forming lesions (104 of 111 lesions) to evaluate the vascularity of the mass, which was one of the BI-RADS criteria for US. Lesion size was defined as the diameter of the hypoechoic lesion at B-mode US.

Images were assigned to one of five categories according to the BI-RADS criteria for US (6): category 1, negative findings; category 2, benign findings; category 3, probably benign findings; category 4, findings suspicious for malignancy; and category 5, findings highly suggestive of malignancy.

Categories were assigned by either the surgeon (E.U.) or the radiologist (E.T.), both of whom were board certified by the Japanese Society of Ultrasonics in Medicine. These investigators determined the BI-RADS category of each lesion, with knowledge of the results of physical examination and mammography but without knowledge of the final pathologic diagnosis.

Elastography.—On the same day, we next obtained elasticity images as motion images, with the patient in the supine position and with the stabilizer-equipped probe oriented perpendicular to the chest wall. The probe was applied to the breast and was moved slightly inferior and superior to obtain the elasticity images.

Importantly, to obtain images that were appropriate for analysis, we applied the probe with only light pressure, which we defined as a level of pressure that maintained contact with the skin and permitted imaging conditions for which the association between pressure and strain was essentially proportional. We avoided using higher levels of pressure, which manifest nonlinear properties of tissue elasticity; in such circumstances, the association between pressure and strain is no longer proportional. It should be

noted, however, that the examiner did not have to maintain a specific level of pressure and that the dynamic range of pressure that was appropriate for elasticity images was wide enough to be controlled with freehand compression. Therefore, the examiner was able to gauge the proper pressure by monitoring the real-time elasticity image while moving the probe. Specifically, if pressure increased above a certain level, the pattern of the elasticity image started to change drastically as the pressure increased; therefore, we did not use images that were obtained above this level of pressure.

In terms of the ROI used for obtaining elasticity images, we set the top of the ROI to include subcutaneous fat and the bottom of the ROI to include a pectoral muscle; lateral borders were set more than 5 mm from the lesion's boundary. The ROI needed to be set to include sufficient surrounding breast tissue because elasticity in this system is displayed relative to the average strain inside the ROI. Ideally, elasticity images are obtained by comparing two images—that is, the one obtained before and the one obtained after compression (described later in more detail). In clinical use, however, multiple frames are acquired, and many elasticity images are generated by comparing two adjacent frames during compression and relaxation by continuously moving the probe. The displacement of these two adjacent frames is usually small (< 0.5 mm). In addition, the process of detecting strain was equivalent to the compensation of the displacement. Consequently, elasticity images were produced by comparing an almost identical area on the two images.

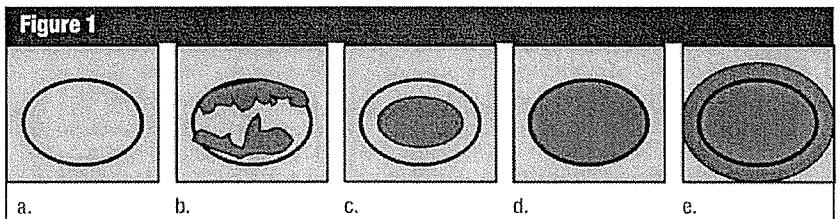

Figure 1: Images present general appearance of lesions for elasticity scores of (a) 1, (b) 2, (c) 3, (d) 4, and (e) 5. Black circle indicates outline of hypoechoic lesion (ie, border between lesion and surrounding breast tissue) on B-mode images.

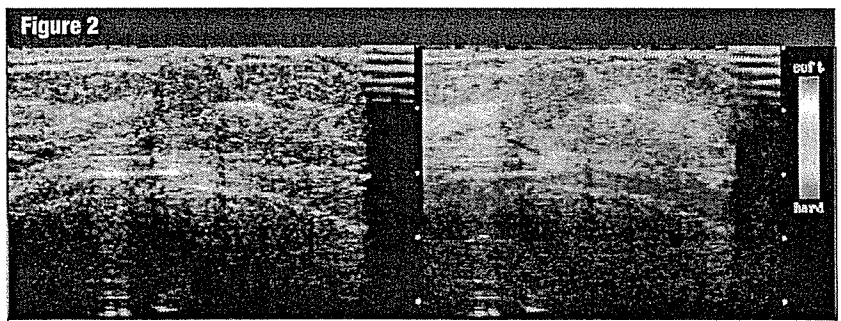

Figure 2: Fibroadenoma with elasticity score of 1 in 51-year-old woman. US images were obtained in transverse plane. Left: On conventional B-mode image, lesion was classified as BI-RADS category 2. Right: On elasticity image, the entire hypoechoic lesion was evenly shaded green, as was the surrounding breast tissue.

Figure 3: Fibroadenoma with elasticity score of 2 in 39-year-old woman. US images were obtained in transverse plane. Left: On conventional B-mode image, lesion was classified as BI-RADS category 3. Right: On elasticity image, hypoechoic lesion shows mosaic pattern of green and blue.

The echo signals acquired by using the US scanner were captured by the external computer and were used to calculate of tissue strain with the CAM. First, the amount of tissue displacement induced by compression was calculated with a two-step process. The first step was the rough estimation of displacement by using the correlation of the envelope (ie, the amplitude) of the radiofrequency signals obtained before and after compression. The purpose of this first step was to avoid the error of aliasing and to determine the approximate displacement in the resolution of the half wavelength.

The second step was the fine estimation of displacement, which precisely determined the displacement from the phase difference of the two echo signals before and after compression. Although the second step resembled that of the Doppler US method, the CAM ensured that aliasing errors did not occur because, as a result of the first step, the difference between the true and estimated displacement was reduced to within a half wavelength. Thus, we were able to obtain a fine estimation of displacement without aliasing error.

Next, strain distribution was ob-

tained from the spatial differentiation of the displacement distribution. The strain distribution was then reconstructed as an elasticity image and was displayed on the computer monitor. The program that was used for this reconstruction was developed at the University of Tsukuba (T.S.) (2–4).

Each pixel of the elasticity image was assigned one of 256 specific colors, depending on the magnitude of strain. The scale ranged from red for components with greatest strain (ie, softest components) to blue for those with no strain (ie, hardest components). Green indicated average strain in the ROI. These color-scale elasticity images were converted to translucent images and were superimposed on the corresponding B-mode images so that the investigator could easily recognize the relationship between strain distribution and the lesion on B-mode images at a glance. Color images were constructed automatically with the same image processing settings throughout the study. Image construction was performed by using a program developed by Hitachi Medical (T.M.) (9).

To obtain a still image for diagnosis, we replayed the recorded motion images and selected an image obtained in the early phase of compression because these images provided the best contrast. Normal breast tissue was displayed in the green range.

To classify elasticity images, we evaluated the color pattern both in the hypoechoic lesion (ie, the area that was hypoechoic or isoechoic relative to the subcutaneous fat [except for echogenic halo] on B-mode images) and in the surrounding breast tissue. On the basis of the overall pattern, we assigned each image an elasticity score on a five-point scale (Fig 1). A score of 1 indicated even strain for the entire hypoechoic lesion (ie, the entire lesion was evenly shaded in green) (Fig 2). A score of 2 indicated strain in most of the hypoechoic lesion, with some areas of no strain (ie, the hypoechoic lesion had a mosaic pattern of green and blue) (Fig 3). A score of 3 indicated strain at the periphery of the hypoechoic lesion, with sparing of the center of the lesion (ie, the peripheral part of lesion was green, and the central part was blue) (Fig 4). A score of 4 indicated no strain in the entire hypoechoic lesion (ie, the entire lesion was blue, but its surrounding area was not included) (Fig 5). A score of 5 indicated no strain in the entire hypoechoic lesion or in the surrounding area (ie, both the

Figure 4

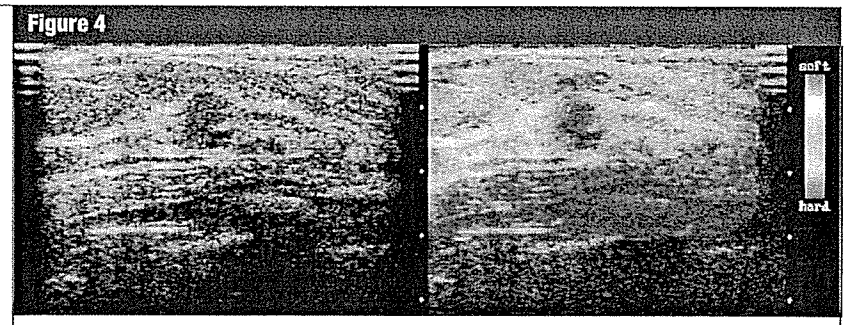

Figure 4: Lobular carcinoma in situ with elasticity score of 3 in 46-year-old woman. US images were obtained in transverse plane. Left: On conventional B-mode image, lesion was classified as BI-RADS category 3. Right: On elasticity image, the central part of the hypoechoic lesion was blue, and the peripheral part of the lesion was green.

Figure 5

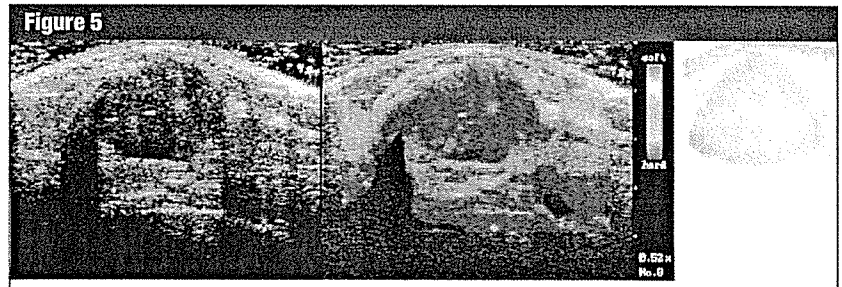

Figure 5: Nonscirrhous type invasive ductal carcinoma with elasticity score of 4 in 29-year-old woman. US images were obtained in transverse plane. Left: On conventional B-mode image, lesion was classified as BI-RADS category 5. Middle: On elasticity image, the entire hypoechoic lesion was blue. Right: Pathologic section of lesion is shown. (Hematoxylin-eosin stain; original magnification, ×1.)

Figure 6

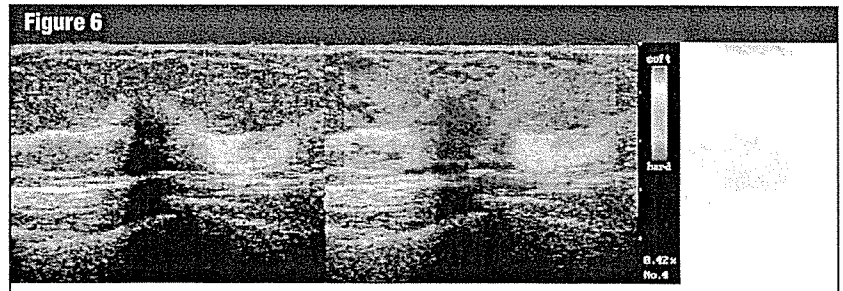

Figure 6: Scirrhous type invasive ductal carcinoma with elasticity score of 5 in 55-year-old woman. US images were obtained in sagittal plane. Left: On conventional B-mode image, lesion was classified as BI-RADS category 5. Middle: On elasticity image, both the entire hypoechoic lesion and its surrounding area were blue. Right: Pathologic section of lesion is shown. (Hematoxylin-eosin stain; original magnification, ×1.)

entire hypoechoic lesion and its surrounding area were blue) (Fig 6).

Scoring was performed by a surgeon (A.I.) who had 5 years of experience in evaluating breast US results according to the imaging patterns described (Fig 1). In the first stage of the study (from March 2002 to March 2003), scoring was performed in 57 lesions, with knowledge of the results of conventional US examination and the final pathologic diagnosis. In the second stage of the study (from April 2003 to September 2003), scoring was performed in 54 lesions, with knowledge of the results of physical examination and mammography but without knowledge of the results of conventional US examination and the final pathologic diagnosis.

Table 2

Final Pathologic Diagnosis in 111 Breast Lesions

Pathologic Diagnosis	No. of Lesions
Malignant lesions	52 (46.8)
Invasive ductal carcinoma	
Nonscirrhous	32 (28.8)
Scirrhous*	10 (9.0)
Ductal carcinoma in situ	9 (8.1)
Mucinous carcinoma	1 (0.9)
Benign lesions	59 (53.2)
ANDI†	24 (21.6)
Fibroadenoma	16 (14.4)
Intraductal papilloma	13 (11.7)
Complex cyst	2 (1.8)
Benign phyllodes tumor†	2 (1.8)
Lobular carcinoma in situ	1 (0.9)
Granuloma	1 (0.9)

Note.—Numbers in parentheses are percentages.

* Defined as carcinoma that had a hard consistency because of excessive production of dense connective tissue.

† Indicates ANDI without fibroadenoma.

‡ Excisional biopsy was performed in both phyllodes tumors; tumors were proven with histologic analysis.

Figure 7

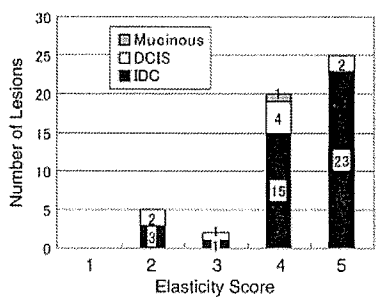

Figure 7: Bar graph demonstrates distribution of elasticity scores for malignant lesions. Numbers on bars indicate the number of lesions. *IDC* = invasive ductal carcinoma, *Mucinous* = mucinous carcinoma.

Statistical Analysis

We first compared malignant and benign lesions by *(a)* comparing the mean elasticity scores for real-time US elasticity images between malignant and benign lesions to determine the score for differentiating between these lesions and *(b)* comparing the elasticity scores between the three groups within each lesion size category (ie, 4–10 mm, 11–20 mm, and 21–30 mm) to assess the usefulness of this modality for various lesion sizes. All comparisons were made by using the Student *t* test.

Furthermore, we compared elasticity scores among the histologic subgroups of lesions by using an analysis of variance (Tukey-type multiple comparison) to assess the correspondence between the elasticity score and the compressibility of each histologic type, with pathologic diagnoses as a reference standard.

Figure 8

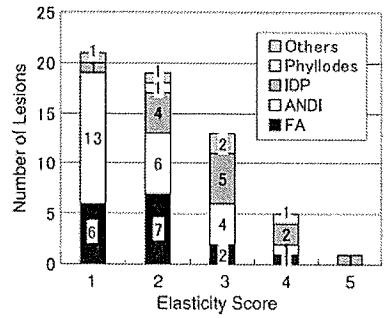

Figure 8: Bar graph demonstrates distribution of elasticity scores for benign lesions. Numbers on bars indicate the number of lesions. For the category termed *others*, lesions included complex cysts, lobular carcinoma in situ, and granulomas. *FA* = fibroadenoma, *IDP* = intraductal papilloma, *Phyllodes* = benign phyllodes tumor.

Finally, we evaluated the ability of the two imaging modalities to allow differentiation of malignant and benign lesions by using a receiver operating characteristic analysis to compare the area under the curve, sensitivity, specificity, and accuracy. Here, the standard proportion test was conducted for sensitivity, specificity, and accuracy. For the indices that did not show a statistically significant difference, we examined equivalence or noninferiority by using the Δ-equivalent test (10).

In addition, we used the χ^2 test to assess the presence of a significant difference between lesions scored in the first stage of the study and those scored in the second stage of the study; as previously noted, the conditions under which scoring was performed were somewhat different.

All statistical tests were performed by using commercially available software (Stat Mate 2000, version 3.01, ATMS, Tokyo, Japan and PASS 2002, NCSS, Kaysville, Utah). For all tests, a *P* value of less than .05 was considered to indicate a statistically significant difference.

Results

Pathologic Diagnoses

Final pathologic diagnoses are shown in Table 2. All breast cancers were diagnosed histologically by means of radical surgery, excisional biopsy, or needle biopsy. Of the 59 benign lesions, 18 were diagnosed at excisional biopsy, 19 at US-guided needle biopsy, and 22 at fine-needle aspiration cytology. Furthermore, all benign lesions remained unchanged during the follow-up period, which spanned more than 1 year.

Elasticity Scores

The distributions of elasticity scores for malignant lesions and benign lesions are shown in Figures 7 and 8, respectively. The mean elasticity score was significantly higher for malignant lesions (4.2 ± 0.9) than for benign lesions (2.1 ± 1.0) ($P < .001$).

Of the 52 malignant lesions, 45 (86%) lesions, including invasive ductal

carcinoma, had a score of 4 or 5. None of the lesions in this group had a score of 1. Of the 59 benign lesions, 40 (68%) lesions, including fibroadenomas and ANDI without fibroadenoma, had a score of 1 or 2 (score of 1, 21 lesions; score of 2, 19 lesions).

One (4%) of the 26 lesions with a score of 5 and five (20%) of the 25 lesions with a score of 4 were benign. Two (13%) of 15 lesions with a score of 3 and five (21%) of 24 lesions with a score of 2 were malignant. Of note, three of the malignant lesions with a score of 2 occurred in the first stage of our study.

The mean elasticity scores according to lesion size on B-mode images are shown in Table 3. For each lesion size category, the mean score was significantly higher for malignant lesions than for benign lesions ($P < .001$).

The distribution of elasticity scores for breast cancers according to their histologic subclassification is shown in Figure 9. The mean score was 3.7 ± 1.0 for DCIS, 4.2 ± 0.9 for invasive ductal carcinoma of nonscirrhous type, and 4.9 ± 0.3 for invasive ductal carcinoma of scirrhous type. There were no significant differences between the mean scores for invasive ductal carcinomas of scirrhous type and those for invasive ductal carcinomas of nonscirrhous type. The mean scores for nonscirrhous carcinoma and those for DCIS did not differ significantly. Mean scores for scirrhous carcinoma and those for DCIS, however, did differ significantly ($P < .05$). Of the five malignant lesions with a score of 2, two were DCIS and three were invasive ductal carcinomas of nonscirrhous type.

The distribution of elasticity scores for benign lesions according to their histologic characteristics is shown in Figure 10. The mean score was 1.9 ± 0.9 for fibroadenoma, 1.7 ± 0.9 for ANDI, and 2.9 ± 1.0 for intraductal papilloma. The mean scores for intraductal papilloma and those for ANDI differed significantly ($P < .01$). In contrast, there was no significant difference between the mean scores for fibroadenoma and those for ANDI or between the mean scores for intraductal papilloma and those for fibroadenoma.

There was no significant difference between the mean elasticity scores for intraductal papilloma and those for DCIS. However, the mean scores for other benign lesions (fibroadenoma and ANDI) and those for all subclasses of carcinomas differed significantly ($P <$ .001 for each comparison).

Diagnostic Performance

Figure 11 shows the receiver operating characteristic curves for elastography and conventional US in differentiating malignant from benign legions. This bar graph shows that the maximum value of the sum of sensitivity and specificity for elastography is higher than that for conventional US. The area under the curve

Table 3

Mean Elasticity Score according to Lesion Diameter

Diameter (mm)*	Malignant	Benign	*P* Value†
4–10	3.9 ± 1.7 (9)	1.9 ± 0.9 (28)	<.001
11–20	4.4 ± 0.8 (27)	2.3 ± 1.2 (26)	<.001
21–30	4.2 ± 1.0 (16)	2.4 ± 0.6 (5)	<.001

Note.—Elasticity scores are presented as the mean ± standard deviation. Numbers in parentheses indicate the total number of lesions for each size category.

* Lesion diameter was determined at B-mode US and was measured to the nearest millimeter.

† Within each size category, the difference between elasticity scores for malignant and benign lesions was determined to be significant by using the Student *t* test.

Figure 9

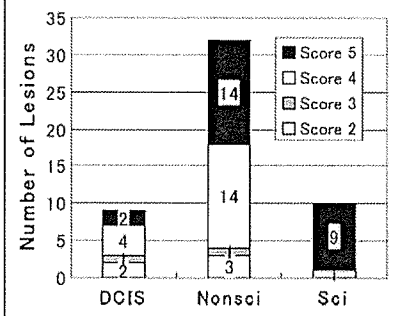

Figure 9: Bar graph demonstrates distribution of elasticity scores for breast cancers according to histologic subclassification. Numbers on bars indicate the number of lesions. *Nonsci* = invasive ductal carcinoma of nonscirrhous type, *Sci* = invasive ductal carcinoma of scirrhous type.

Figure 10

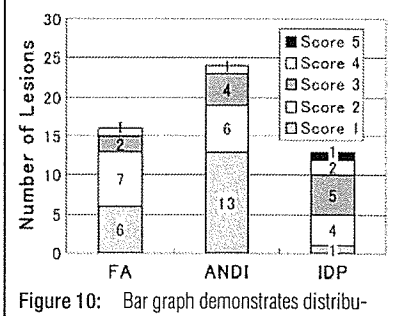

Figure 10: Bar graph demonstrates distribution of elasticity scores for benign lesions according to histologic subclassification. Numbers on bars indicate the number of lesions. *FA* = fibroadenoma, *IDP* = intraductal papilloma.

Figure 11

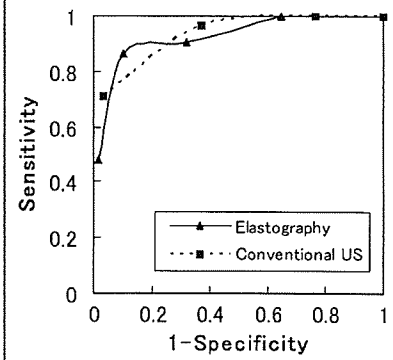

Figure 11: Receiver operating characteristic curves for elastography and conventional US. The area under the curve was almost the same for both elastography and conventional US (0.9185 and 0.9153, respectively). Statistical comparison was not possible because the number of lesions was insufficient.

for elastography was 0.9185, which is slightly higher than that for conventional US (0.9153).

The diagnostic performance of conventional US and of elastography at various cutoff points for the entire study period (stage one and stage two) is shown in Table 4. For elastography, sensitivity (86.5% [45 of 52]; 95% confidence interval: 77.3%, 83.5%), specificity (89.8% [53 of 59]; 95% confidence interval: 82.1%, 97.5%), and accuracy (88.3% [98 of 111]; 95% confidence interval: 82.3%, 94.3%) are shown, with the best cutoff point between elasticity scores of 3 and 4. According to the conventional method, a cutoff point is defined as best if it attains the maximum of value of sum of sensitivity and specificity. The sensitivity (71.2% [37 of 52]; 95% confidence interval: 58.8%, 83.5%), specificity (96.6% [57 of 59]; 95% confidence interval: 92.0%, 100.0%), and accuracy (84.7% [94 of 111]; 95% confidence interval: 78.0%, 91.4%) of conventional US are also shown in Table 4, with the best cutoff point between BI-RADS category 4 and 5. If another cutoff point is applied between BI-RADS category 3 and 4, then sensitivity moves to 96.2% (50 of 52), specificity to 62.7% (37 of 59), and accuracy to 78.4% (87 of 111).

By applying the best cutoff point for each image, we found that elastography had a higher sensitivity than conventional US ($P < .05$). Elastography had lower specificity and lower accuracy than conventional US, but these differences were not significant. Therefore, when we considered the equivalence band, the specificity of elastography was not inferior to (ie, not more than 15% different than) ($P < .05$) and accuracy was equivalent to (ie, within 13% of) ($P < .05$) that of conventional US.

When the conventional US cutoff point was set between BI-RADS category 3 and 4, only two lesions had false-negative results, but 22 lesions had false-positive results. More than half of the false-positive lesions (14 [64%] of 22 lesions) had elasticity scores of 1 or 2 (score of 1, nine lesions; score of 2, five lesions). When the conventional US cutoff point was set between BI-RADS category 4 and 5, only two lesions had false-positive results, but 15 lesions had false-negative results. More than half of the false-negative lesions (11 [73%] of 15 lesions) had elasticity scores of 4 or 5 (score of 4, eight lesions; score of 5, three lesions).

In contrast, when the cutoff point for elastography was set between scores of 3 and 4, the majority of the false-negative results at elastography (six [86%] of seven lesions) were for lesions with a BI-RADS category of 4 or 5 (category 4, three lesions; category 5, three lesions); the one remaining lesion was classified as BI-RADS category 3. Of the six false-positive findings at elastography, three were for BI-RADS category 4 lesions, one was for a BI-RADS category 3 lesion, and two were for BI-RADS category 2 lesions.

In the first stage of the study, the sensitivity, specificity, and accuracy of elastography were 89.3% (25 of 28), 93.1% (27 of 29), and 91.2% (52 of 57), respectively, with a cutoff point of between 3 and 4. Also in the first stage of the study, the sensitivity, specificity, and accuracy of conventional US were 78.6% (22 of 28), 93.1% (27 of 29), and 86.0% (49 of 57), respectively, with a cutoff point of between 4 and 5.

In the second stage of the study, the sensitivity, specificity, and accuracy of elastography were 83.3% (20 of 24), 86.7% (26 of 30), and 85.2% (46 of 54), respectively, with a cutoff point of between 3 and 4. For conventional US, the sensitivity, specificity, and accuracy were 62.5% (15 of 24), 100% (30 of 30), and 83.3% (45 of 54), respectively, with a cutoff point of between 4 and 5. There was no significant difference between the first and second stage of the study with respect to the sensitivity, specificity, and accuracy of elastography and conventional US ($P > .05$). Therefore, we combined results for the two stages of subsequent analyses.

Table 4

Sensitivity, Specificity, and Accuracy of Elastography and Conventional US at Various Cutoff Points for the Diagnosis of Benign and Malignant Lesions

Cutoff Point*	Sensitivity (%)	Specificity (%)	Accuracy (%)
Elasticity score			
Between 1 and 2	100 (52/52)	35.6 (21/59)	65.8 (73/111)
Between 2 and 3	90.4 (47/52)	67.8 (40/59)	78.4 (87/111)
Between 3 and 4	86.5 (45/52)	89.8 (53/59)	88.3 (98/111)
Between 4 and 5	48.1 (25/52)	98.3 (58/59)	74.8 (83/111)
Conventional US category†			
Between 1 and 2	100 (52/52)	0 (0/59)	46.8 (52/111)
Between 2 and 3	100 (52/52)	23.7 (14/59)	59.5 (66/111)
Between 3 and 4	96.2 (50/52)	62.7 (37/59)	78.4 (87/111)
Between 4 and 5	71.2 (37/52)	96.6 (57/59)	84.7 (94/111)

Note.—Numbers in parentheses were used to calculate percentages.

* Cutoff points are presented for the entire study period (ie, for stage one and stage two).

† Conventional US category was defined according to the BI-RADS classification for US.

Discussion

Investigators have performed freehand US elastography in patients with breast lesions by using off-line assessment and have compared the traced outlines of tumors on B-mode images with those on grayscale elastograms (11,12). Although our method is similar to theirs, we were able to make an elasticity assessment instantly because our scoring system was simple; as a result, we believe our system is more practical for clinical use. A freehand US elastography system that permits real-time assessment has been developed and clinically tested. The freehand system uses spatial correlation and has rapid signal processing (12); however, the CAM provides a higher frame rate while maintaining high image quality. The other system uses a one-dimensional search; as a result, the performance of this sys-

tem can be compromised by lateral movement of the probe (11).

From a diagnostic point of view, our findings concur with those of other studies—namely, that elastography is useful for characterizing breast lesions in general and has the potential to allow differentiation between malignant and benign lesions (1,11–13). In the clinical setting, grayscale US elastography during which patients are imaged in a seated position has been performed for those with breast lesions, and motor-driven compression plates have been used (1). Investigators have reported that elastography allowed differentiation of cancers from fibroadenomas, and that the width of the cancers was greater on elasticity images than on B-mode images. Our results, which are derived with the more clinically practical freehand approach, correspond with theirs. In addition, we believe that our system is more rapid for demonstrating longitudinal displacement and more robust for lateral movement of the probe. With our system, lesions can be easily found because translucent color-scale elasticity images are superimposed on the corresponding B-mode images.

Clinical Implications

Although we are not yet able to precisely quantitate elasticity, we have arrived at a point where semiquantitative assessment in the clinical setting is possible.

Our finding of a significant difference between mean elasticity scores for malignant and benign lesions in patients suggests that elastography may be useful in diagnosing breast lesions in the clinical setting. Moreover, this discriminatory capability did not depend on lesion size when lesions were smaller than 30 mm in diameter. The mean elasticity score for scirrhous carcinoma was significantly higher than that for DCIS, and the mean scores for fibroadenoma and ANDI were lower than those for carcinomas. These results agree with experimental results for elastic moduli, as measured in vitro (14).

We believe that an elasticity score of 5, which shows no strain in the entire hypoechoic lesion and the surrounding area at B-mode US, indicates infiltration of cancer cells into the interstitial tissues (eg, in scirrhous carcinomas) or into an intraductal component (eg, in DCIS), both of which are characteristics of carcinoma.

An elasticity score of 4, which indicates no strain in the entire hypoechoic lesion, seems to be characteristic of tumors such as solid tubular carcinomas that are circumscribed and homogeneously harder than the adjacent normal breast tissue.

In our study, an elasticity score of 3, which indicates strain at the periphery of the hypoechoic lesion, was mainly found in benign lesions, including intraductal papillomas. The importance of strain at the periphery is unclear at present and requires further investigation. We recommend that all lesions with elasticity scores of 3 or higher be examined by means of aspiration cytology or needle biopsy because two (13%) of the 15 lesions with a score of 3 were malignant.

We believe that elasticity scores of 2, for which parts of the hypoechoic lesion did not show strain at B-mode US, indicate lesions that are soft yet somewhat harder than normal breast tissue. This is often characteristic of lesions such as fibroadenoma or ANDI. Of the five malignant lesions with scores of 2, two were DCIS and three were invasive ductal carcinomas at histologic analysis. Investigators have noted that DCIS is softer than invasive ductal carcinoma (14). The finding of a lower elasticity score in lesions suspicious for DCIS is therefore plausible and suggests that correct diagnosis of these lesions will require the use of other imaging modalities in addition to elastography.

Three patients with invasive ductal carcinoma had lesions with a score of 2, but we found no specific histologic features to explain the lower elasticity score in these patients. These false-negative results may have resulted from an artifact that was created by applying the probe with too much pressure during elastography. Two of these lesions were examined in the first stage of our study, and the examiner did not grasp the probe with an appropriate level of pressure. All of the invasive ductal carcinomas with a score of 2 (three lesions) were classified as BI-RADS category 4 or 5, a finding that supports the combined use of elastography and conventional US to avoid misdiagnosing an invasive carcinoma as a benign lesion.

We believe that an elasticity score of 1, which shows even strain in the entire hypoechoic lesion at B-mode US, indicates that lesions have almost the same compressibility as the surrounding breast tissue. In our study, no malignant lesions had a score of 1. Although our findings will require confirmation, this result suggests that invasive diagnostic procedures, such as histologic examination, may be omitted for patients who have lesions with a score of 1.

The result of our receiver operating characteristic curve analysis suggests that elastography may have a diagnostic performance that is better than, or at least equal to, that of conventional US, with the best cutoff point in the means of high sensitivity. Both accuracies coincide with each other within a 13% difference, and the specificity of elastography was not inferior to (ie, not more than 15% different than) that of conventional US. These results show that, compared with conventional US, elastography has higher sensitivity, a noninferior specificity of no more than 15%, and an equivalent accuracy of within 13%, which encourages us to believe that the results were obtained with elastography only. Because classifying elasticity images with our scoring system is simpler than classifying images with a scoring system based on the BI-RADS criteria for conventional US, we believe that even an examiner with limited training may be able to obtain the same diagnostic performance as an experienced examiner with elastography.

Of particular note, 14 (64%) of 22 patients who had false-positive results and a conventional US cutoff point of between BI-RADS category 3 and 4 had elasticity scores of 1 or 2; at minimum, the nine patients with a score of 1 could have conceivably been spared further procedures. In addition, we believe that, with concomitant use of elastogra-

phy and conventional US, it may be possible to downgrade some BI-RADS category 3 and 4 lesions to BI-RADS category 2 lesions. As a result, this approach may reduce the number of false-positive results and unnecessary invasive diagnostic procedures.

Limitations

Our study has some limitations. Patients with cancer were overrepresented because our hospital serves as a referral center for general clinics. Therefore, the findings cannot necessarily be extended to the general population. In addition, the lesions that were assessed were predominantly larger lesions. Although elastography facilitated the differentiation of malignant lesions from benign lesions (even among lesions smaller than 10 mm), few lesions in this study were smaller than 5 mm. Therefore, further studies on the use of elastography for the characterization of small lesions will be necessary.

Elastography itself, like all imaging modalities, has certain limitations. The main pitfall of this modality is that the extent of tissue compression influences both the elasticity image and, consequently, the elasticity score. When elasticity scores are used for diagnosis, images obtained with the application of strong pressure may lead to misdiagnosis. Images with minimal perturbation of strain relationships can be obtained by lightly pressing the probe to the breast. It takes some practice to be able to exert light pressure on the same cross-sectional surface of the breast. Of note, three (60%) of five false-negative results obtained by using an elasticity score cutoff point of between 3 and 4 occurred during the first stage of our study when the examiner was just getting used to the probe operation. We cannot, however, determine if the pressure was inappropriate because there is currently no pressure indicator available. Until a pressure gauge becomes available, examiners must attempt to apply the probe with light pressure by monitoring the real-time image to obtain images that are appropriate for elasticity analysis. Another shortcoming is that, although most images clearly resemble one of the five distinct patterns used for classification, the selection is currently made by the examiner and is not yet automated.

In conclusion, we believe that elastography can complement conventional US, thereby making it easier to diagnose breast lesions. Our experience suggests that the skill needed to acquire adequate images is similar for conventional US and elastography; the skill needed to interpret images, however, is somewhat less for elastography when our classification system is used. Elastography is promising, and we expect that with future improvements in the technology (eg, the development of a pressure indicator and approaches for quantitative assessment), this imaging modality will become an invaluable tool for the diagnosis of breast diseases in the clinical setting.

Acknowledgment: We thank Susan London, MS, Biomedical Writing and Editing, Seattle, for the correction of our manuscript.

References

1. Garra BS, Cespedes EI, Ophir J, et al. Elastography of breast lesions: initial clinical results. Radiology 1997;202:79–86.
2. Shiina T, Doyley MM, Bamber JC. Strain imaging using combined RF and envelope autocorrelation processing. In: Proceedings of the IEEE Ultrasonics Symposium. Savoy, Ill: Institute of Electrical and Electronics Engineers Ultrasonics, Ferroelectrics, and Frequency Control Digital Archive, 1996;2: 1331–1336.
3. Shiina T, Nitta N, Ueno E, Bamber JC. Real time tissue elasticity imaging using the combined autocorrelation method. J Med Ultrason 2002;29:119–128.
4. Nitta N, Yamakawa M, Shiina T, Ueno E, Doyley MM, Bamber JC. Tissue elasticity imaging based on combined autocorrelation method and 3-D tissue model. In: Proceedings of the IEEE Ultrasonics Symposium. Savoy, Ill: Institute of Electrical and Electronics Engineers Ultrasonics, Ferroelectrics, and Frequency Control Digital Archive, 1998;2: 1447–1450.
5. Yamakawa M, Shiina T. Strain estimation using the extended combined autocorrelation method. Jpn J Appl Phys 2001;40:3872–3876.
6. American College of Radiology. Breast imaging reporting and data system (BI-RADS), ultrasound. 4th ed. Reston, Va: American College of Radiology, 2003. Available at: http://www.acr.org/s_acr/sec.asp?CID=882&DID=14550. Accessed September 8, 2004.
7. Japanese Breast Cancer Society. General rules for clinical and pathological recording of breast cancer. 15th ed. Tokyo, Japan: Japanese Breast Cancer Society, 2002.
8. Hughes LE. The ANDI concept and classification of benign breast disorders: an update. Br J Clin Pract Suppl 1989;68:1–6.
9. Matsumura T, Tamano S, Mitake T, et al. Development of freehand ultrasound elasticity imaging system and in vivo results. In: Proceeding of the 1st International Conference on the Ultrasonic Measurement and Imaging of Tissue Elasticity. Rochester, NY: University of Rochester, 2002;1:80.
10. Tango T. Equivalence test and confidence interval for the difference in proportions for the paired-sample design. Stat Med 1998; 17(8):891–908.
11. Hiltawsky KM, Kruger M, Starke C, et al. Freehand ultrasound elastography of breast lesions: clinical results. Ultrasound Med Biol 2001;27:1461–1469.
12. Hall TJ, Zhu Y, Spalding CS. In vivo real-time freehand palpation imaging. Ultrasound Med Biol 2003;29:427–435.
13. Krouskop TA, Younes PS, Srinivasan S, Wheeler T, Ophir J. Differences in the compressive stress-strain response of infiltrating ductal carcinomas with and without lobular features: implications for mammography and elastography. Ultrason Imaging 2003;25: 162–170.
14. Krouskop TA, Wheeler TM, Kallel F, Garra BS, Hall T. Elastic moduli of breast and prostate tissue under compression. Ultrason Imaging 1998;20:260–274.

Japanese Journal of Applied Physics
Vol. 45, No. 5B, 2006, pp. 4740–4748

Pressure Gradient Estimation Based on Ultrasonic Blood Flow Measurement

Naotaka NITTA*, Kazuhiro HOMMA and Tsuyoshi SHIINA[1]

Institute for Human Science and Biomedical Engineering, National Institute of Advanced Industrial Science and Technology (AIST), 1-2-1 Namiki, Tsukuba, Ibaraki 305-8564, Japan
[1]*Graduate School of Systems and Information Engineering, University of Tsukuba, 1-1-1 Tennoudai, Tsukuba, Ibaraki 305-8573, Japan*

(Received November 30, 2005; revised February 26, 2006; accepted March 1, 2006; published online May 25, 2006)

Mechanical load to the blood vessel wall, such as shear stress and pressure, which occurs in blood flow dynamics, contribute greatly to plaque rupture in arteriosclerosis and to biochemical activation of endothelial cells. Therefore, noninvasive estimations of these mechanical loads are able to provide useful information for the prevention of vascular diseases. Although the pressure is the dominant component of mechanical load, for practical purposes, the pressure gradient is also often important. So far, we have investigated the estimation of the kinematic viscosity coefficient using a combination of the Navier-Stokes equations and ultrasonic velocity measurement. In this paper, a method for pressure gradient estimation using the estimated kinematic viscosity coefficient is proposed. The validity of the proposed method was investigated on the basis of the analysis with the data obtained by computer simulation and a flow phantom experiment. These results revealed that the proposed method can provide a valid estimation of the pressure gradient. [DOI: 10.1143/JJAP.45.4740]

KEYWORDS: vessel wall, mechanical loads, blood velocity measurement, kinematic viscosity coefficient, pressure gradient

1. Introduction

Mechanical load to the blood vessel wall, such as shear stress and pressure, which occurs in blood flow dynamics, contribute greatly to plaque rupture in arteriosclerosis and to biochemical activation of endothelial cells.[1–7] Therefore, noninvasive estimations of these mechanical loads are able to provide useful information for the prevention of vascular diseases.

Mechanical load to the blood vessel wall as a result of blood flow is roughly classified by the tangential force and the force normal to the vessel wall. Here, the tangential and normal forces correspond to shear stress and pressure, respectively. Pressure is the dominant component in mechanical load because its magnitude is much larger than that of shear stress. On the other hand, for practical purposes, the pressure gradient is often more important than the pressure itself. For example, the pressure loss produced at the stenosed part due to arteriosclerosis plaque is frequently calculated using the Doppler velocity measurement and the simplified Bernoulli equation. Since the pressure loss is defined by the differential pressure between two points, the pressure loss corresponds to the pressure gradient, which is the spatial gradient of the pressure distribution. Therefore, the pressure gradient calculation of the blood flow is important and useful when analyzing the blood flow dynamics.

We have investigated a method for estimating the kinematic viscosity coefficient of fluid using a combination of the Navier-Stokes equations and ultrasonic velocity vector measurement.[8] Moreover, a method for assessing the intravascular shear stress has also been investigated on the basis of the estimated kinematic viscosity coefficient under the assumption of a known density.[9] In addition, an assessment with respect to pressure is necessary for completing the hemodynamics analysis.

The conventional method for estimating the pressure gradient is based on the Stokes equation, assuming unidirectional flow, and the application of the least-squares method to all velocity data within the flow field.[10] Therefore, it is difficult to obtain the intravascular distribution of the pressure gradient.

In this study, by extending the previous method for estimating the kinematic viscosity coefficient, a method for estimating the pressure gradient and its distribution is developed, without the assumption of unidirectional flow, on the basis of a combination of the Navier-Stokes equations and the ultrasonic velocity vector field. The validity of this method is investigated by using analyzing data obtained by computer simulation and a flow phantom experiment.

This paper is structed as follows. In §2, a method for estimating the pressure gradient on the basis of the kinematic viscosity coefficient estimation is proposed. In §3 and §4, the analysis results of the data obtained by simulation and experiment are presented. In §5, we discuss the conclusions.

2. Principle of Pressure Gradient Estimation

It is assumed that blood is an isotropic and incompressible viscous fluid and that the velocity vector distribution has already been obtained in the palmic phase in which Newtonian properties can be assumed.

Here, in view of practicality, a two-dimensional (2D) flow state is treated. More detailed theory of the three-dimensional (3D) flow state is discussed in the appendix. In the 2D flow state, the pressure gradient components in the Cartesian coordinate system can be described, on the basis of the Navier-Stokes equations, as follows:

$$\frac{\partial p}{\partial x} = \rho(\nu X - U), \tag{1}$$

$$\frac{\partial p}{\partial y} = \rho(\nu Y - V), \tag{2}$$

where ρ and ν are the density and the kinematic viscosity coefficient, respectively. U, V, X, and Y are defned only by velocity vector components, (u, v), as

$$U = \frac{\partial u}{\partial t} + u\frac{\partial u}{\partial x} + v\frac{\partial u}{\partial y}, \tag{3}$$

$$V = \frac{\partial v}{\partial t} + u\frac{\partial v}{\partial x} + v\frac{\partial v}{\partial y}, \tag{4}$$

*E-mail address: n.nitta@aist.go.jp

$$X = \frac{\partial^2 u}{\partial x^2} + \frac{\partial^2 u}{\partial y^2}, \tag{5}$$

$$Y = \frac{\partial^2 v}{\partial x^2} + \frac{\partial^2 v}{\partial y^2}. \tag{6}$$

On the other hand, the kinematic viscosity coefficient ν can be derived, by eliminating the pressure terms in eqs. (1) and (2), as[8]

$$\nu = \frac{\dfrac{\partial \xi}{\partial t} + u\dfrac{\partial \xi}{\partial x} + v\dfrac{\partial \xi}{\partial y}}{\dfrac{\partial^2 \xi}{\partial x^2} + \dfrac{\partial^2 \xi}{\partial y^2}}, \tag{7}$$

where ξ is the vorticity defined as

$$\xi = \frac{\partial v}{\partial x} - \frac{\partial u}{\partial y}. \tag{8}$$

Since we assume an incompressible fluid, there is no spatial gradient of the density, and the density is constant in the flow field. Therefore, by assuming a known density, the pressure gradients can be obtained by substituting the kinematic viscosity coefficient of eq. (7) into eqs. (1) and (2). This means that the pressure gradients can be obtained from only the velocity vector distribution.

Although a 2D velocity vector distribution is necessary for obtaining the pressure gradients, only one velocity component along the beam axis can be measured by the present ultrasonic Doppler method. In order to obtain the component orthogonal (lateral) to the beam axis, the incompressible condition can be adopted.[8] Therefore, a 2D velocity vector distribution can be composed by the measurement of the beam axis component by the ultrasonic Doppler method and the estimation of the lateral component under the incompressible condition.

On the other hand, $\nabla p = (\partial p/\partial x, \partial p/\partial y)$ means a vector in the Cartesian coordinate system because the pressure p is a scalar. This means that the pressure gradients vary according to the assignment of the Cartesian coordinate. In the ultrasonic measurement, the beam direction could be adopted as one axis in the Cartesian coordinate system. In other words, the pressure gradients vary according to the positioning of the ultrasonic probe. Therefore, for the independent assessment of probe positioning, it is promising to calculate the pressure gradient along the tangential direction of the streamline, which is the curve whose tangential vector corresponds to the velocity vector. Therefore, by transforming the coordinate system so that one of the directional vectors along the original Cartesian coordinate axes determined by probe positioning agrees with the velocity vector direction, the tangential pressure gradient of the streamline can be obtained. Since ∇p is a vector, the coordinate transformation due to rotation can be applied to obtain the tangential pressure gradient.

In the Cartesian coordinate system shown in Fig. 1, the pressure gradient vector $(\partial p/\partial x, \partial p/\partial y)$ in the O–xy system determined by probe positioning can be transformed to the vector $(\partial p/\partial x', \partial p/\partial y')$ in the O'–$x'y'$ system, as follows:

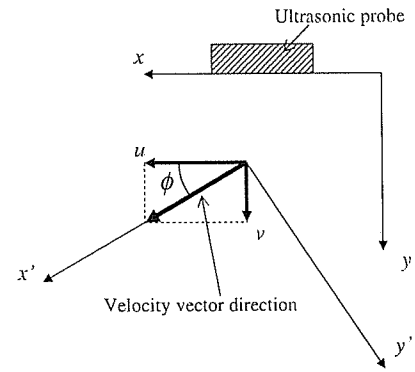

Fig. 1. Cartesian coordinate system determined by the position of the ultrasonic probe and its coordinate transformation by rotation.

$$\begin{pmatrix} \dfrac{\partial p}{\partial x'} \\ \dfrac{\partial p}{\partial y'} \end{pmatrix} = \begin{pmatrix} \cos\phi & \sin\phi \\ -\sin\phi & \cos\phi \end{pmatrix} \begin{pmatrix} \dfrac{\partial p}{\partial x} \\ \dfrac{\partial p}{\partial y} \end{pmatrix}. \tag{9}$$

In Fig. 1, since the coordinate system is transformed such that the x' axis agrees with the tangential direction of the streamline, the tangential pressure gradient can be obtained as

$$\frac{\partial p}{\partial x'} = \frac{\partial p}{\partial x}\cos\phi + \frac{\partial p}{\partial y}\sin\phi. \tag{10}$$

The rotation angle ϕ is obtained from the velocity vector. In Fig. 1, when the x' axis agrees with the velocity vector direction, the v' component along the y' axis becomes zero in the transformed O'–$x'y'$ system. Using this relationship, each component of the transformation matrix in eq. (9) can be denoted, with the velocity vector components, as

$$\cos\phi = \frac{u}{V}, \tag{11}$$

$$\sin\phi = \frac{v}{V}, \tag{12}$$

where V is the absolute value of the velocity vector and is defined by $V = \sqrt{u^2 + v^2}$. Finally, by substituting eqs. (11) and (12) into eq. (10), the tangential pressure gradient of the streamline can be derived as

$$\frac{\partial p}{\partial x'} = \frac{\partial p}{\partial x}\frac{u}{V} + \frac{\partial p}{\partial y}\frac{v}{V}. \tag{13}$$

This means that the tangential pressure gradient can be derived by using the pressure gradient vector and the velocity vector in the original coordinate system determined by the probe position, without cumbersome calculation concerning the rotation angle ϕ.

3. Simulation Analysis

The validity of the proposed method for estimating the pressure gradients was investigated by simulation analysis. As shown in Fig. 2, a 3D flow model with a step imitating the arteriosclerosis plaque structure, where the vorticity required for estimating the kinematic viscosity coefficient was arisen, was considered. The principle described in §2 involves a method based on the 2D velocity vector distribution from the viewpoint of practicality and this

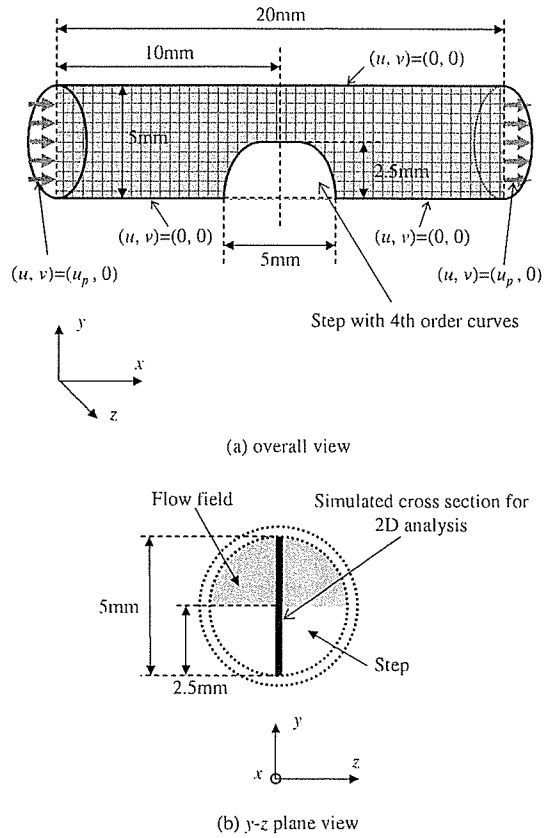

Fig. 2. Flow model for simulation. (a) Overall view of the model and (b) short-axis cross section of the tube on the y–z plane.

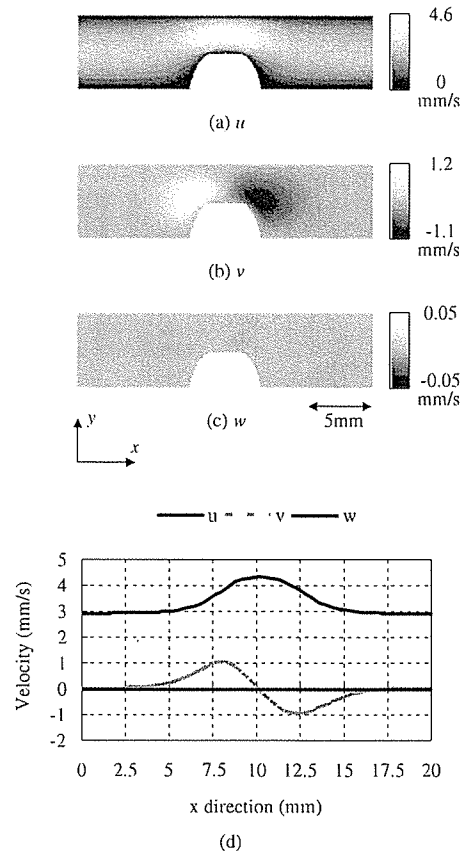

Fig. 3. Three-dimensional velocity vector components on the central cross section obtained by 3D finite element method. (a) x, (b) y, and (c) z components of the velocity vector distribution on the central cross section are shown, which are indicated as u, v, and w, respectively. (d) Vector component profiles of u, v and w on the central tube axis.

corresponds to the z component of the 3D velocity vector being neglected around the x–y cross section on the central tube axis shown in Fig. 2. Therefore, if the z component of the velocity vector on the x–y cross section is much smaller than the other components, it is expected that the actual pressure gradient on the same cross section can be estimated more accurately even if that estimation is based only on the 2D velocity vector.

In order to evaluate the magnitude of the z component on the x–y cross section, a 3D finite element method (FEM) was applied to the 3D flow model shown in Fig. 2. Although this model has a configuration similar to that of the previously investigated model,[8] the boundary conditions are different from the previous conditions. That is, the fixed boundary conditions at which the velocity vectors become 0 on the wall with the step, and the natural boundary conditions under which the velocity vectors are perpendicular to the faces at the inlet and the outlet of the model, are imposed. Navier–Stokes equations with a realistic kinematic viscosity coefficient (around $3.0\,\mathrm{mm^2/s}$) and density ($10^3\,\mathrm{kg/m^3}$) were solved by iterative FEM calculation, and the distributions of 3D velocity vector components on the cross section were obtained. A small initial value of the velocity component along the x axis was provided so that the iterative calculation would converge stably. The results are shown in Fig. 3 for (a) x, (b) y, and (c) z components of the velocity vector distribution on the cross section, where these components are indicated as u, v, and w, respectively. Figure 3(d) also shows the vector component profiles of u, v, and w on the central tube axis. As shown in Fig. 3, the total magnitude of w is much smaller than that of the other u and v distributions and is close to 0. The w distribution also exhibits an almost uniform pattern. This indicates that, for achieving more accurate estimation based on the 2D velocity vector alone, it is appropriate to use the 2D velocity vector distribution obtained on the central cross section in this tube structure. In order to avoid the huge computation time of the 3D FEM, in the following analysis, the 2D flow field analysis, in which the z component of the velocity vector is neglected, can be effectively performed by the finite difference method, based on the above findings of the 3D analysis. The 2D flow field analysis was performed on the x–y cross section, as shown in the dark area of Fig. 2, and the 2D velocity vector distributions were obtained. Here, the same boundary conditions as in the above 3D analysis were also used. In the following simulation, assuming that the 2D velocity vector distributions have already been obtained by ultrasonic measurements, the pressure gradients were estimated using the 2D velocity vector distributions obtained by this finite difference method.

Figure 4 shows the analysis results obtained with the kinematic viscosity coefficient of $3.0\,\mathrm{mm^2/s}$, where (a) and (b) display the streamline and the vorticity distributions, respectively. In the streamline, a valid distribution can be attained along the boundary configurations. In the vorticity

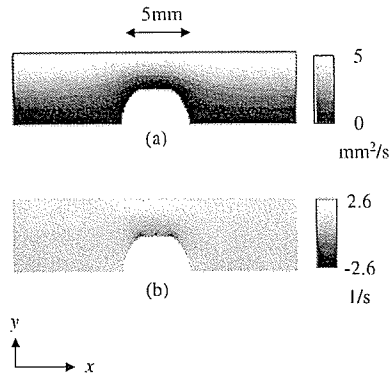

Fig. 4. (a) Streamline and (b) vorticity distributions obtained by the finite difference method.

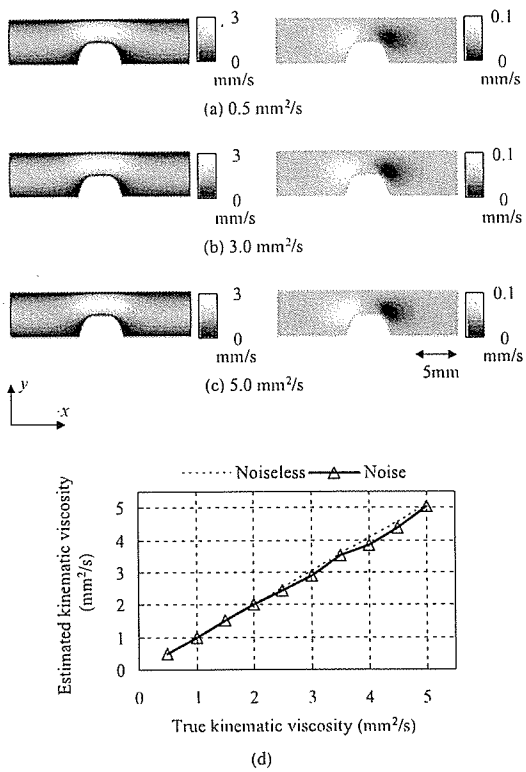

Fig. 5. Velocity vector distributions corresponding to the kinematic viscosity changes and the estimated result of the kinematic viscosity coefficient. In (a) to (c), left panels indicate the x-component distributions of the velocity vector (u), and right panels indicate the y-component distributions of the velocity vector (v). Each component of the velocity vector was obtained on the basis of the original Cartesian coordinate system. (d) True and the estimated values of the kinematic viscosity coefficients. Horizontal axis indicates the true values and the vertical axis indicates the estimated values.

distribution, it can be observed that the vorticity rises around the step.

Figure 5 shows the velocity vector distributions with the kinematic viscosity coefficients changed from 0.5 to 5.0 mm^2/s, and the results of the kinematic viscosity coefficients estimated using the velocity vector distributions. The broken line indicates the estimated result when the ideal velocity vector distributions without noise were utilized, and

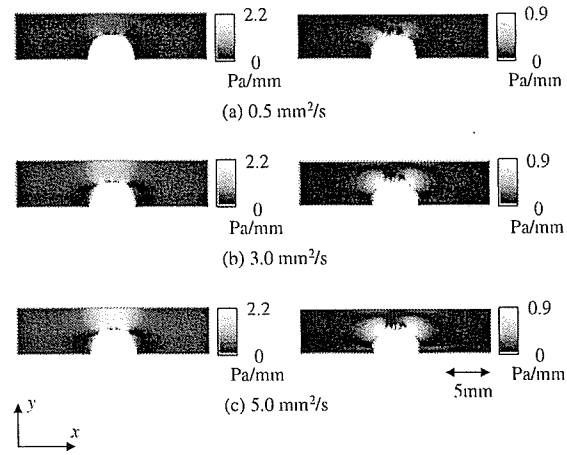

Fig. 6. Ideal pressure gradient distributions obtained using the velocity vector distributions without noise, corresponding to kinematic viscosity changes. In (a) to (c), left panels indicate the x-component distributions of the pressure gradient ($\partial p/\partial x$), and right panels indicate the y-component distributions of the pressure gradient ($\partial p/\partial y$). Each component of the pressure gradient was obtained on the basis of the original Cartesian coordinate system.

the solid line indicates the estimated result when the velocity vector distributions with white noise, which simulate those obtained by ultrasonic measurement, were utilized. Here, the amplitude of white noise was set to 40 dB lower than the maximum absolute value of the ideal velocity vector, and this white noise was added to each ideal velocity vector component. Similarly to the previous results,[8] valid kinematic viscosity estimations could be obtained.

Figure 6 shows the ideal pressure gradient distributions obtained using the velocity vector distributions without noise when the kinematic viscosity coefficients were changed from 0.5 to 5.0 mm^2/s. Since the velocity vector data were obtained on the square grids in this simulation, the difference width was set to 0.2 mm along both x and y directions in calculating eqs. (3) to (6) by the central difference method, and the pressure gradient distribution was attained. Each component of the pressure gradient obtained on the basis of the original Cartesian coordinate system is displayed. In this case, the pressure gradients become larger according to the kinematic viscosity increase. Also, it can be observed that the pressure gradients around the step are larger than those in other regions.

Figure 7 shows the tangential pressure gradient $\partial p/\partial x'$ distributions estimated using the velocity vector distributions and the pressure gradients, $\partial p/\partial x$ and $\partial p/\partial y$, when the kinematic viscosity coefficients were changed from 0.5 to 5.0 mm^2/s. These results show the pressure gradient acting along the streamlines shown in Fig. 4(a). Left panels indicate the ideal tangential pressure gradient obtained using the ideal velocity vector distributions without noise and the true kinematic viscosity coefficient, and right panels indicate the estimated tangential pressure gradient obtained using the velocity vector distributions with the same white noise as that in the case of Fig. 5 and the estimated kinematic viscosity coefficient. Dynamic ranges in all images are standardized. Estimated distributions coincide well with the ideal distributions. Figure 7(d) shows the comparison be-